Stony Brook University

OFFICIAL COPY

The official electronic file of this thesis or dissertation is maintained by the University Libraries on behalf of The Graduate School at Stony Brook University.

© All Rights Reserved by Author.

Properties of Adiabatic Rapid Passage Sequences

A Thesis Presented

by

Benjamin Simon Gläßle

to

The Graduate School

in Partial Fulfillment of the Requirements

for the Degree of

Master of Arts

in

Physics

Stony Brook University

August 2009

Stony Brook University

The Graduate School

Benjamin Simon Gläßle

We, the thesis committee for the above candidate for the Master of Arts degree, hereby recommend acceptance of this thesis.

Harold J. Metcalf – Thesis Advisor
Distinguished Teaching Professor, Department of Physics and Astronomy

Todd Satogata
Adjunct Professor, Department of Physics and Astronomy

Thomas H. Bergeman
Adjunct Professor, Department of Physics and Astronomy

This thesis is accepted by the Graduate School.

Lawrence Martin
Dean of the Graduate School

Abstract of the Thesis

Properties of Adiabatic Rapid Passage Sequences

by

Benjamin Simon Gläßle

Master of Arts

in

Physics

Stony Brook University

2009

Adiabatic rapid passage (ARP) sequences can be used to exert optical forces on neutral atoms, much larger than the radiative force. These sequences consist of counter-propagating and synchronized optical pulses whose frequency is swept through the resonance of the transition.

The new results from the numerical studies discussed in chapter 3 shall be pointed out. The numerical integration of the optical Bloch equations show a superior stability of the force, when alternate sweep directions are used. This discovery was investigated in the parameter space of ARP and under various perturbations.

The experiment was setup for two optical beamlines, whose parameters can be controlled individually. This allows us to do velocity capture range measurements or compare other variations of our scheme.

To those who boldy go where no one has gone before.

Contents

List of Figures viii

List of Tables x

Acknowledgements xi

1 Introduction 1
1.1 Two-level atoms 2
1.1.1 Schrödinger Equation 2
1.1.2 Rabi-Oscillations 5
1.1.3 The Optical Bloch Equations 8
1.1.4 Dressed Atom Picture 10
1.2 Traditional Optical Forces 12
1.2.1 Radiative Force 13
1.2.2 Optical Molasses 14
1.3 Bichromatic Force 15
1.4 Properties of Helium 21

2 Theory of Adiabatic Rapid Passage Sequences 23
2.1 Adiabatic Rapid Passage 24
2.2 Non-adiabatic Transition Probability 27
2.3 Periodicity 29
2.4 Force from Periodic ARP Sequences 34

3 Numerical Simulations 37
3.1 Effects of Spontaneous Emission 38
3.1.1 Force Distribution 40
3.2 Velocity dependence 41
3.2.1 Capture range 43
3.3 Sweep direction 44
3.3.1 Non-constant peak Rabi frequency 48

3.3.2 Random phases 48

4 Vacuum System 50
4.1 Beamline 50
4.1.1 Metastable Helium source 52
4.2 Interaction 55
4.3 Detection 55

5 Generation of ARP Light 60
5.1 Laser 60
5.1.1 Laser-Locking by SAS 62
5.2 Electro optic effect 64
5.2.1 Phase Modulation 67
5.2.2 Amplitude Modulation 69
5.3 Light Analysis 72
5.4 Light Setup 75

6 Measurement of the Force 78
6.1 Deflection 78
6.2 Parameters 80
6.3 Setup 82
6.3.1 Observation of ARP 83
6.3.2 Capture range measurements 84
6.3.3 Comparison of sweep directions 85

7 Conclusion 86

Bibliography 88

A Code 92
A.1 Definition of the Optical Bloch Equations 92
A.2 Numerical Integration 97

List of Figures

1.1 Two Level System 4
1.2 Rabi-Oscillation 7
1.3 Bloch-sphere 9
1.4 Dressed Energy levels 11
1.5 Light shift 12
1.6 Radiative Push 15
1.7 Force-profile of optical molasses 16
1.8 π-pulse model 16
1.9 Energies of the doubly dressed Hamiltonian 20
1.10 Energy levels of Helium 22

2.1 Dressed energy trajectory 25
2.2 Adiabatic following of the Bloch vector 26
2.3 Non-adiabatic transition probability map 31
2.4 Bloch-vector trajectories 32
2.5 Periodic behavior of the trajectory endpoints 33
2.6 Pulse scheme 35

3.1 Capture-range map without decay 40
3.2 Approximate force map 41
3.3 Force-distribution 42
3.4 Velocity dependence of the ARP-force 43
3.5 Capture range of the ARP force 44
3.6 Velocity dependence of the force 45
3.7 Integrated P_{nad} 46
3.8 Effects of random phases 49

4.1 Diagram of the vacuum system 51
4.2 Metastable reverse flow source 52
4.3 Velocity distribution of our metastable Helium beam 54
4.4 Interaction region schematics 56
4.5 MCP/PS Detector 57

5.1 Extended cavity setup 62
5.2 Saturation absorption spectroscopy setup 63
5.3 Electro optic coordinate system 65
5.4 Modulator layout 67
5.5 Calibration curve for PM2 70
5.6 Characteristics of a Mach-Zehnder interferometer 71
5.7 Calculated FP spectra of modulated light 73
5.8 Light analysis data 74
5.9 ARP modulation scheme 76
5.10 ARP interaction layout 77

6.1 Distribution of the inverse and squared velocity 79
6.2 Undeflected atom-beam 80
6.3 Deflection image of the detector 83

List of Tables

1.1 Properties of the relevant He* transitions 21

Acknowledgements

This work and this year would have never been possible without several people. And it definitely would not have been that much fun!

First of all I want to thank my advisor Hal Metcalf that he accepted me into his group and for his broad support. I generally appreciate all the help and fun our group contributed and want mention two people individually. Jason Reeves had to listen to almost any experimental question I was confronted with and was helpful even if he did not knew the answer. And to Dan Stack whom I was working with on the ARP experiment: Thank you for putting up with me. I also want to acknowledge everyone from the machine shop, especially Mark and Jeffrey T. . Pat and Laszlo helped to master all administrative stumbling blocks. My committee was patient and very helpful.

All the "Germans' were ready for anything and made me feel not that far from home. My accompanying exchange students from Würzburg Benedikt and Stefan were terrific house mates. Rene "brightened" my prospect with his opinions. Tin and other fellow students were and hopefully will continue to be good friends whom I had a lot of fun with.

I am thankful for the support of the German government and the exchange program of the University of Würzburg, which is run by Prof. Assaad.

My family superbly supported me. Finally and especially I thank Raphaela for enduring my absence and her support.

Chapter 1

Introduction

The motional control of single, neutral atoms is difficult, because there is no simple mechanical interaction which can be used to manipulate them. The invention of the laser made it possible to address single, distinct transitions. Different kinds of elements can be distinguished and addressed individually.

The momentum transfer between light and atoms allows us to manipulate the motion of atoms. This can be used to cool atoms and trap them [1], or to collimate neutral atom beams [2]. Cooling atoms down to near the motional ground state of a trap allows us to access regimes which are heavily investigated nowadays: Doppler-free spectroscopy up to the point where transitions can be used as an atomic clock, and Bose Einstein condensation or cold fermions.

Traditional optical forces are dependent on the decay rate of the used transistion, which limits their magnitude. Much greater forces can be achieved when absorption and stimulated emission are used. This has been demonstrated for the bichromatic [3] and the adiabatic rapid passage (ARP) force [4]. The latter one is the subject of this thesis. ARP requires multiple optical

pulses, whose frequency is swept through resonance. This thesis shows numerical results that predict the force to be more stable in case of alternating sweep directions.

In this chapter I give a brief introduction into the interaction of light and neutral atoms, traditional optical forces and the bichromatic force. Chapter 2 is about the theory of ARP. This is followed by the discussion of the numerical studies in Ch. 3 and their findings. Chapters 4, 5 and 6 describe the experiment, which was set up to test the discoveries of Ch. 3.

1.1 Two-level atoms

For the purpose of ARP the consideration of only two levels is necessary. There are several ways to describe this system, which will be introduced in the following sections.

1.1.1 Schrödinger Equation

The time-dependent Schrödinger-Equation describes the quantum state of neutral atoms in any environment

$$\mathrm{i}\hbar\frac{\partial\psi(\vec{r},t)}{\partial t} = \mathcal{H}(t)\psi(\vec{r},t) \tag{1.1}$$

In the absence of external fields, especially radiation fields, the Hamiltonian $\mathcal{H}(t)$ becomes time-independent $\mathcal{H}(t) = \mathcal{H}_0$. $\mathcal{H}_0$ is diagonal yielding $\mathcal{H}_0\phi_k = E_k\phi_k$. These ϕ_k form a complete set of eigenfunctions, therefore the total

(time-dependent) wave-function $\psi(\vec{r}, t)$ can be expanded as

$$\psi(\vec{r}, t) = \sum_k c_k(t)\phi_k(\vec{r}) \exp(-\mathrm{i}\omega_k t) \tag{1.2}$$

The presence of a radiation field can be treated as a perturbation: the Hamiltonian becomes

$$\mathcal{H}(t) = \mathcal{H}_0 + \tilde{\mathcal{H}}(t) \tag{1.3}$$

where the interaction between radiation field and atomic system is described by the term $\tilde{\mathcal{H}}(t)$.

Upon inserting into Eq. (1.2) the Schrödinger Equation becomes

$$\begin{aligned} \mathcal{H}(t)\psi(\vec{r}, t) &= \left[\mathcal{H}_0 + \tilde{\mathcal{H}}(t)\right] \sum_k c_k(t)\phi_k(\vec{r}) \exp(-\mathrm{i}\omega_k t) \\ &= \mathrm{i}\hbar \left(\frac{\partial}{\partial t}\right) \sum_k c_k(t)\phi_k(\vec{r}) \exp(-\mathrm{i}\omega_k t) \end{aligned} \tag{1.4}$$

After multiplying with $\phi_j^*(\vec{r})$ from the right and removing all spatial components by integrating over them, the generalized Schrödinger Equation becomes

$$\mathrm{i}\hbar \frac{\mathrm{d}c_j(t)}{\mathrm{d}t} = \sum_k c_k(t)\tilde{\mathcal{H}}_{jk}(t) \exp(\mathrm{i}\omega_{jk} t), \tag{1.5}$$

where the transition $j \to k$ is described in terms of its resonance frequency $\omega_{jk} = (\omega_j - \omega_k)$ and the matrix element $\tilde{\mathcal{H}}_{jk}(t) = \langle \phi_j | \tilde{\mathcal{H}}(t) | \phi_k \rangle$,

This problem can not be solved analytically. Near resonant monochromatic laser light strongly couples two distinct levels. Provided that, during the time of the experiment, there are no other levels the system can decay to, it is possible to neglect all other levels. The remaining two levels are coupled by

the laser light with frequency $\omega_l = \omega_a + \delta$, where $\omega_a = \omega_{jk}$ is the resonance-frequency of the transition and δ is the detuning of the laser frequency ω_l from resonance. The energetically lower state is called the ground state $|g\rangle$ and the other one the excited state $|e\rangle$.

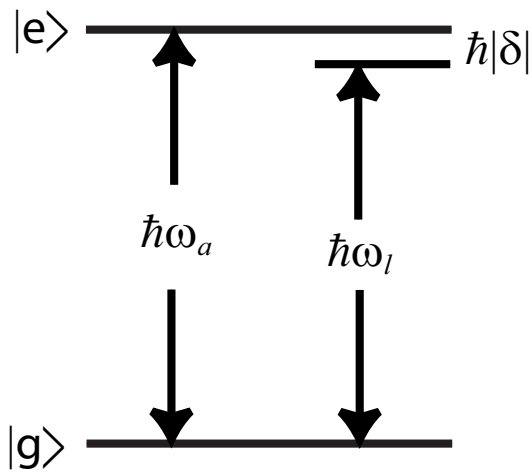

Figure 1.1: Relevant energies in a two level system. The system with resonance frequency ω_a is driven by a laser field oscillating at ω_l which is detuned by δ. Taken out of [5].

The quantum state is described by $|\psi(t)\rangle = c_e(t)|e\rangle + c_g(t)|g\rangle$ or the vector $\vec{\psi}(t) = (c_e(t), c_g(t))^\intercal$. Any diagonal elements of $\tilde{\mathcal{H}}(t)$ are absorbed into $\mathcal{H}_0$, leaving only the transition elements $\tilde{\mathcal{H}}_{ge} = \tilde{\mathcal{H}}^*_{eg}$. The remaining, coupled equations describe the well known Rabi problem [6, 7]

$$\mathrm{i}\hbar \frac{\mathrm{d}c_g(t)}{\mathrm{d}t} = c_e(t)\tilde{\mathcal{H}}_{ge}(t)\exp(-\mathrm{i}\omega_a t) \tag{1.6a}$$

and

$$\mathrm{i}\hbar \frac{\mathrm{d}c_e(t)}{\mathrm{d}t} = c_g(t)\tilde{\mathcal{H}}_{eg}(t)\exp(\mathrm{i}\omega_a t). \tag{1.6b}$$

1.1.2 Rabi-Oscillations

In a semi-classical approach [8] the interaction term can be written as

$$\tilde{\mathcal{H}}(t) = -e\vec{r} \cdot \vec{E}(\vec{r}, t) \tag{1.7}$$

where the electric dipole $e\vec{r}$ of the atom couples to electric field $\vec{E}(\vec{r}, t)$ of the radiation field. The electron's relative position to the nucleus is described by the vector $\vec{r}$. This describes the system in surprisingly great detail.

Two approximations: The laser wavelength is of the order of several hundreds of nano-meters, whereas the wave-function of the atom is almost completely contained within a few Bohr radii a_0. The electric field the atomic system experiences can therefore be treated as spatially constant $\vec{E}(\vec{r}, t) \rightarrow \vec{E}(t)$. This is the so called electric dipole approximation. Upon defining

$$\Omega = \frac{-eE_0}{\hbar} \hat{e} \cdot \langle e|\vec{r}|g\rangle \tag{1.8}$$

as the resonant Rabi-frequency, the interaction can be described by the off-diagonal elements of the Hamiltonian $\tilde{\mathcal{H}}_{eg}(t) = \tilde{\mathcal{H}}^*_{ge}(t) = \hbar\Omega\cos(\omega_l t)$.

These elements consist of two oscillatory counter-propagating components. Considering the explicit phases in Eqs. 1.6 there are going to be two oscillatory terms in each differential equation. One is going to be oscillating at the frequency of the detuning δ. The other one is going to be highly oscillatory at approximately twice the laser frequency. The rotating wave approximation (RWA) neglects these highly oscillatory terms since none of the other components change on the same timescale and its time-average is zero [9]. Studies

on the dropped, highly oscillatory term show that it gives rise to a small shift in the resonance frequency, the so called Bloch-Siegert shift [10], which can be neglected for our purposes. Additionally to that, we perform a rotating frame transformation, to dispose any remaining complex terms. Equivalent to the whole procedure is to take the solutions

$$c_g(t) = a_g(t) \tag{1.9a}$$

$$c_e(t) = a_e(t)\mathrm{e}^{\mathrm{i}\delta t}. \tag{1.9b}$$

Thereby Eqs. (1.6) transform into another system of differential equations for $a_{g,e}(t)$

$$\mathrm{i}\,\dot{a}_g(t) = \frac{\Omega}{2}\left(1 + \mathrm{e}^{-\mathrm{i}2\omega_l t}\right) a_e(t) \tag{1.10a}$$

$$\mathrm{i}\,\dot{a}_e(t) = -\delta a_e(t) + \frac{\Omega}{2}\left(1 + \mathrm{e}^{\mathrm{i}2\omega_l t}\right) a_g(t) \tag{1.10b}$$

We can clearly identify two fast oscillating terms and drop them. For convenience I will from here on write $c_{g,e}(t)$ again, but will be truly referring to the transformed $a_{g,e}(t)$.

These transformed variables can be used to uncouple Eqs. (1.6). The resulting 2nd order differential equations can be solved. Assuming that the atom was initially in the ground state ($c_g(t=0) = 1$ and $c_e(t=0) = 0$) the time dependent coefficients become

$$c_g(t) = \left(\cos\frac{\Omega' t}{2} - \mathrm{i}\frac{\delta}{\Omega'}\sin\frac{\Omega' t}{2}\right)\exp(\mathrm{i}\delta/2) \tag{1.11a}$$

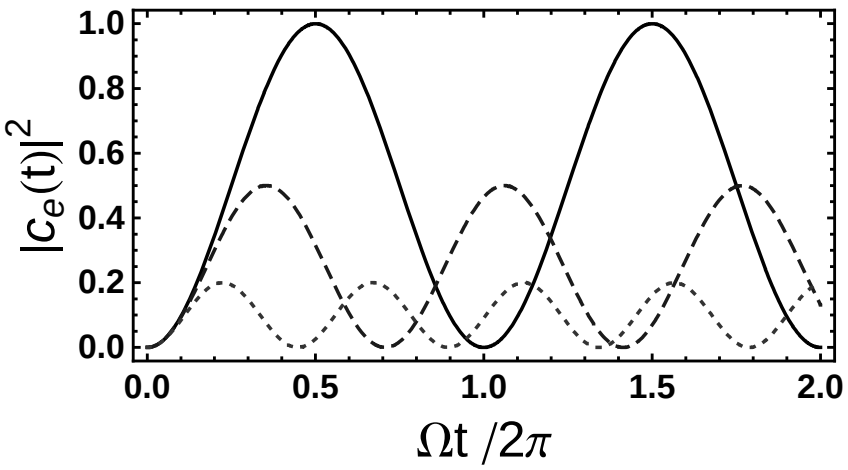

Figure 1.2: Oscillation of the probability to be in the excited state for different detunings. The full (dashed,dotted) line is for $\delta = 0\,(\Omega, 2\Omega)$ detuning.

and

$$c_e(t) = -\mathrm{i}\frac{\Omega}{\Omega'}\sin\frac{\Omega' t}{2}\exp(-\mathrm{i}\delta/2) \tag{1.11b}$$

where $\Omega' = \sqrt{\Omega^2 + \delta^2}$ is the generalized Rabi-frequency, at which the two-level system oscillates between ground and excited state.

The Hamiltonian for the "new" states $c_{g,e}(t)$ becomes

$$\mathcal{H} = \frac{\hbar}{2}\begin{pmatrix} -2\delta & \Omega^* \\ \Omega & 0 \end{pmatrix} \tag{1.12}$$

Using a slightly different transformation than Eqs. (1.9) results in shifted diagonal elements $(-\delta, \delta)$ such that the trace becomes zero, without any effects on the underlying physics.

1.1.3 The Optical Bloch Equations

Two complex numbers $c_g(t)$ and $c_e(t)$ describe the time-dependence of our atomic system. An alternate description of the atomic system was introduced by [11] and a good discussion can also be found in [9, 10]. Instead of Eqs. (1.6) we can use the density matrix

$$\rho = |\psi\rangle\langle\psi| = \begin{pmatrix} |c_e|^2 & c_e c_g^* \\ c_g c_e^* & |c_g|^2 \end{pmatrix} \tag{1.13}$$

to describe our system. This matrix can be decomposed into a basis, consisting of the identity matrix $\mathbf{1}$ and the three Pauli matrices σ_i. Using Einstein's summing convention it becomes

$$\rho = \frac{1}{2}\left(r_0\mathbf{1} + r_i\sigma_i\right) \tag{1.14}$$

with $r_0 = |c_g|^2 + |c_e|^2 = 1$, the probability to observe the atom in either one of the states. The other coefficients are

$$r_1 = \quad c_g c_e^* + c_g^* c_e \tag{1.15a}$$

$$r_2 = \quad \mathrm{i}\left(c_e c_g^* - c_g c_e^*\right) \tag{1.15b}$$

$$r_3 = \quad |c_e|^2 - |c_g|^2 \tag{1.15c}$$

These three variables form the Bloch-vector $\vec{R} = (r_1, r_2, r_3)^\intercal$, which is normalized $|\vec{R}| = |c_e|^2 + |c_g|^2 = 1$. It always stays on the unit sphere, the so called Bloch-sphere.

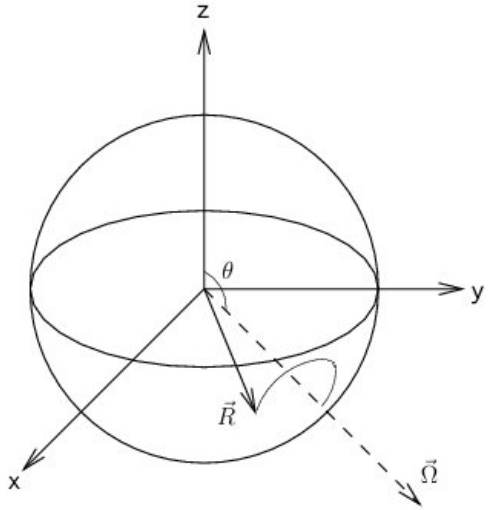

Figure 1.3: Bloch-sphere representation of a two level system coupled by near resonant light. The probability difference to be in either one of the states is represented by the vertical component of the Bloch vector, where as the relative phase of the two states is expressed in the azimuthal angle. The presence of a light field creates a torque around which the Bloch vector precesses. Taken out of [12].

The time-dependence of these new variables is described according to the Heisenberg picture (for not specifically time-dependent operators). If we decompose our Hamiltonian into the Pauli matrices $\mathcal{H} = \Omega_i \sigma_i$, we get the following solution

$$\begin{aligned} \dot{r}_i &=< \dot{\sigma}_i >= \mathrm{Tr}\big[\, \mathrm{i}[\sigma_i, \mathcal{H}]\, \rho \,\big] \\ &= \frac{\mathrm{i}\Omega_j}{2}\, \mathrm{Tr}\Big[\, [\sigma_i, \sigma_j]\, (r_0 \mathbf{1} + r_k \sigma_k) \,\Big] \\ &= \varepsilon_{ijk} \Omega_j r_k. \end{aligned} \tag{1.16}$$

The time dependence is described geometrically by the well known vector cross

product

$$\frac{\mathrm{d}\vec{R}}{\mathrm{d}t} = \vec{\Omega} \times \vec{R}, \tag{1.17}$$

where the torque vector is defined by $\vec{\Omega}(t) = (\mathrm{Re}\,\Omega(t), \mathrm{Im}\,\Omega(t), -\delta(t))^{\intercal}$. This result can be confirmed by substituting Eq. (1.10) into the time-derivative of Eqs. (1.15). The Rabi-frequency is generally complex, but the Bloch-sphere can be rotated such that $\mathrm{Im}\,\Omega(t) = 0$. This representation provides great insight into any kind of two level system, since its parameters correlate more to real measures than the complex amplitudes $c_{g,e}(t)$. Furthermore it is a completely real, 3D master vector equation, whose numerical integration does not pose any major problems.

The Bloch-sphere picture is widely used, since it applies to any kind of two level system. Transformations in quantum computing are often described by it [13].

1.1.4 Dressed Atom Picture

Instead of treating the light as a perturbation to the atomic system, we can include the modes of the radiation field into the Hamiltonian of our system

$$\mathcal{H} = \mathcal{H}_a + \mathcal{H}_{rad} + \mathcal{H}_{int} \tag{1.18}$$

where $\mathcal{H}_a$ is the usual atomic Hamiltonian, $\mathcal{H}_{rad} = \hbar\omega_l\big(a^\dagger a + 1/2\big)$ accounts for the modes of the radiation field and $\mathcal{H}_{int}$ describes the interaction as discussed in Sec. 1.1.2. The energy-structure of the complete Hamiltonian is shown in Fig. 1.4. Note the almost degenerate levels $2, n-1$ and $1, n$. These mix due to

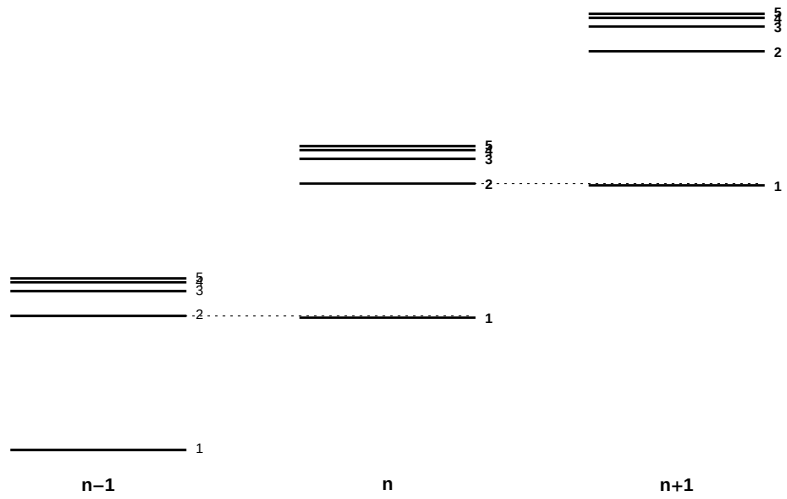

Figure 1.4: Dressed extension of the the atomic Hamiltonian. Note that the (2, n-1)- and the (1,n)-level are only degenerate if the light is on resonance.

the interaction term and the eigenstates $|\phi_{1,2}\rangle$ of the diagonalized Hamiltonian become

$$|\phi_1\rangle = \cos\theta|g\rangle - \sin\theta|e\rangle \tag{1.19a}$$

$$|\phi_2\rangle = \sin\theta|g\rangle + \cos\theta|e\rangle. \tag{1.19b}$$

These are the so called dressed states, where θ is the mixing angle defined by $\cos 2\theta = \frac{-\delta}{\Omega'}$. The corresponding Eigen-energies of this Hamiltonian are : $E_{1,2} = -\delta \pm \sqrt{\delta^2 + \Omega^2}$. The energy-shift for small $\Omega \ll |\delta|$ is

$$\Delta E_{1,2} \approx \mp \frac{\hbar\Omega^2}{4\delta} \tag{1.20}$$

This is the so called light shift, shown in Fig. 1.5. In case of a spatially dependent light field, such as a standing wave configuration, a potential arises,

which is periodic over one wavelength. It is repulsive (attractive) at the nodes for negative (positive) detuning δ. This can be used for optical lattices or for state dependent force schemes, since each state experiences a different potential.

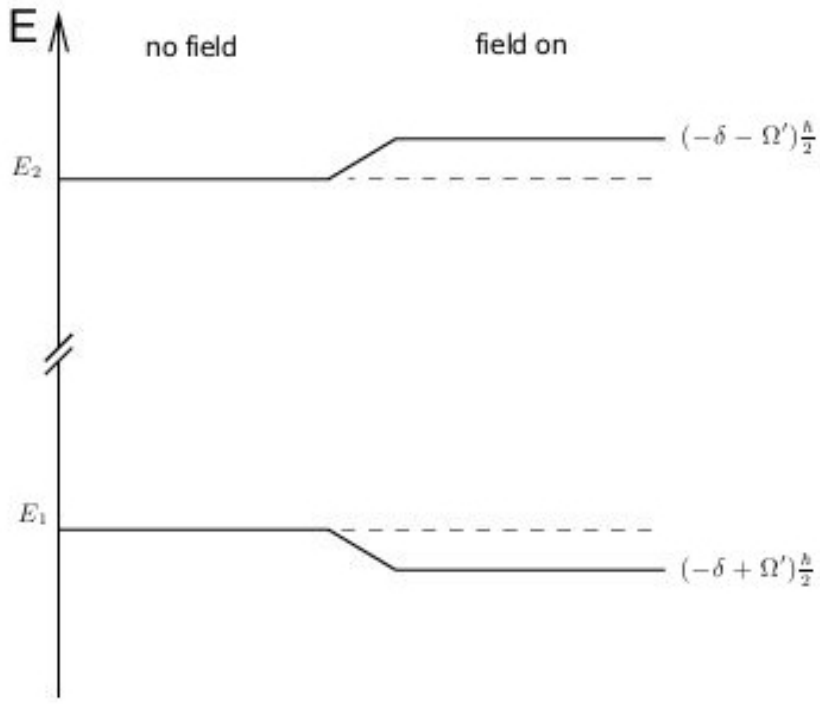

Figure 1.5: The presence of a radiation field shifts the Eigen-energies of the Hamiltonian. Figure taken out of [12].

1.2 Traditional Optical Forces

The controlled momentum transfer between atom and light allows one to exert forces on atoms. Various schemes exist and can be used to control the motion of atoms. The discussion follows [14].

1.2.1 Radiative Force

When monochromatic light close to or on resonance interacts with an atom at rest, a photon is absorbed with a certain probability depending on the strength of the transition and the intensity of the light, which is usually easily saturated. When this happens the momentum of the photon $\hbar k$ is transferred to the atom, where $\vec{k}$ is the wavenumber of the incident laser light. Due to vacuum fluctuation this excited state of the atom decays with a probability of e^{-1} in the time $\tau = \gamma^{-1}$ back to its ground state and sends out a photon in a random direction. The parameter τ is called the life time of the transition. As soon as the atom is in the ground state again the process can repeat. The momentum transfer of the atom by the spontaneously emitted photon averages to zero, since every direction is as likely as the others. We therefore are able to push the atoms in the propagation direction of our laser light. The force experienced by an atom from this laser light is

$$\vec{F} = \gamma_p \hbar \vec{k}, \tag{1.21}$$

where $\gamma_p = \gamma \rho_{ee}$ is the scattering rate, consisting of decay rate γ and time average population probability of the excited state

$$\rho_{ee} = \frac{s}{2(1+s)} = \frac{s_0/2}{1 + s_0 + (2\delta/\gamma)^2} \tag{1.22}$$

which can be expressed in terms of a saturation parameter $s = \frac{s_0}{1+(2\delta/\gamma)^2}$. The saturation parameter $s_0 = \frac{2|\Omega|^2}{\gamma^2} = \frac{I}{I_{sat}}$ at resonance can be interpreted as trade-off between the decay rate γ and the rate at which the system is driven.

$I_{sat} = \frac{\pi \mathrm{hc}}{3\lambda^3\tau}$ is the saturation intensity, characteristic for the specific two-level system with lifetime τ. A detuning δ from resonance decreases the effective coupling dependent on the width of the transition which behaves like the decay rate γ.

In the case of moving atoms we have to transfer to rest-frame of the atom. Doing this yields, in case of atoms moving along the direction of the light, a Doppler shifted frequency $\omega' \approx \omega - \vec{k} \cdot \vec{v}$. The detuning has to be modified $\delta \rightarrow \delta' = \delta - \vec{k} \cdot \vec{v}$:

$$\vec{F}_{rad} = \frac{s_0\gamma/2}{1 + s_0 + \Big(2\big(\delta - \vec{k} \cdot \vec{v}\big)/\gamma\Big)^2}\hbar\vec{k} \tag{1.23}$$

indicates the important aspects of the final result, maximal force is $\vec{F} = \frac{\gamma\hbar\vec{k}}{2}$, which is clearly limited by the lifetime of the excited state $\tau = 1/\gamma$. Towards high intensities nonlinear effects begin to matter and this formalism can no longer be applied.

1.2.2 Optical Molasses

By purposefully red-detuning our light we shift the center of the force towards atoms which are moving against the light direction. If we retro-reflect we can add a negative force at maximum for atoms moving against the retro-reflected beam. The maximum force from the two beams occur at equally spaced velocities from the originally true resonance at $v = 0$. A force profile for a certain set of parameters ($\delta = -\gamma$ and $\Omega = \gamma$) is shown in Fig. 1.7.

Adding this setup in all 3 dimensions allows one to efficiently cool atoms to

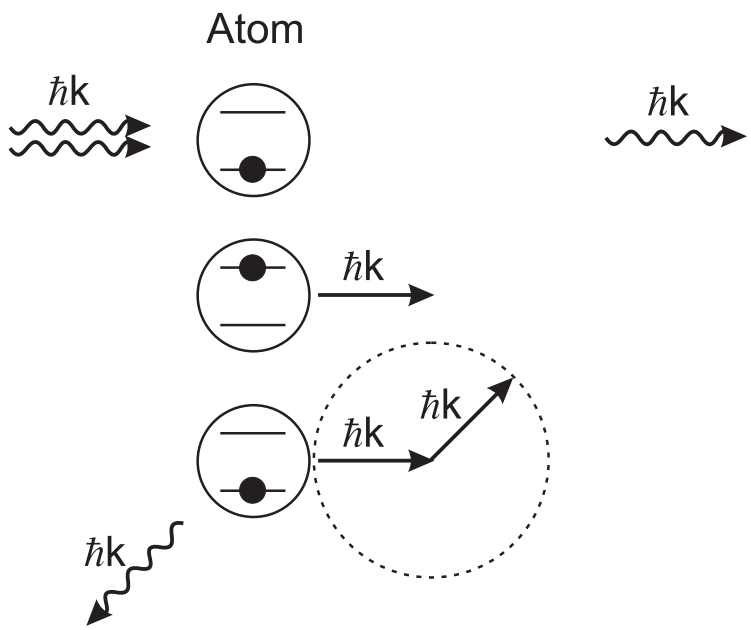

Figure 1.6: Atoms are excited by a laser field. The momentum of the light is transfered onto the atom. The excited state of the atom decays back into the ground state and emits a photon in a random direction. The recoil momentum kick averages to zero over many absorption processes. Figure out of [15].

low temperatures. The lowest temperature achievable is $T_D = \frac{\hbar\gamma}{2k_B}$. Cooling to lower temperature can be achieved by other schemes. Every scheme is limited by the fact, that the atom always receives one final momentum kick. The result is that the the lowest velocity is the recoil velocity $v_r = \hbar k/m$.

1.3 Bichromatic Force

So far the biggest constraint on optical forces has been the fact that they were dependent on the spontaneous decay rate γ. Suppose that an absorption process from one beam is followed by a stimulated emission into a counter-propagating beam; the net momentum transfer would be $\Delta p = 2\hbar k$ into the

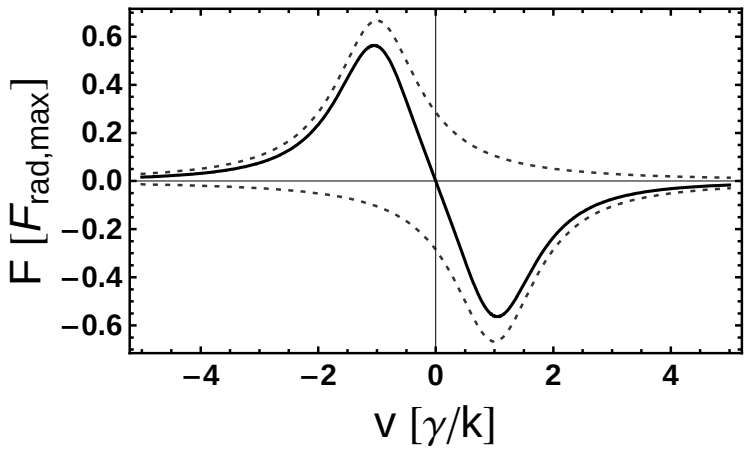

Figure 1.7: Calculated force profile for optical molasses with detuning $\delta = -\gamma$ and saturation parameter $s = 2$. The dashed line are the individual components of each beam and the solid line is their sum.

direction of the first beam. Using monochromatic light to do this results in a standing wave configuration, where the sequence could be started in either order and will therefore average to zero. This limitation can be overcome by the use of two or more frequencies. The bichromatic force is irreversible, strong and has a large capture range compared to any of the traditional optical forces.

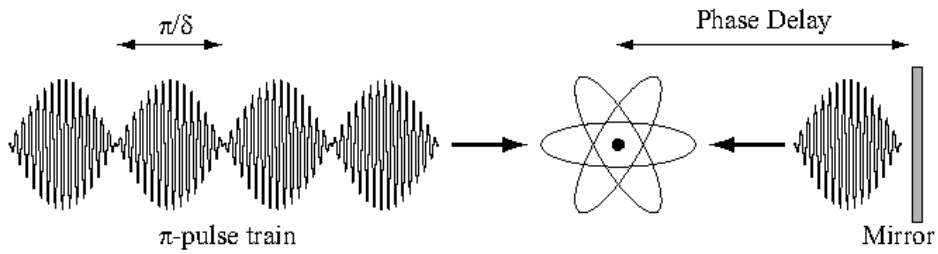

Figure 1.8: A two level system is driven into the excited state by absorption from a pulse of the right propagating beam and driven back via stimulated emission from a pulse propagating to the left. The effective momentum transfer is $2\hbar k$. Taken out of [12].

A simple picture which gives first insight into the bichromatic force is the π-pulse model [16, 17]. Two co-propagating light fields of equal intensity have oppositely detuned frequencies $\omega_{1,2} = \omega_a \pm \delta$, resulting in a beat envelope of the electric field

$$E(t) = E_0 \left[\cos(\omega_1 t) + \cos(\omega_2 t)\right] = 2E_0 \cos(\delta t) \cos(\omega_a t). \tag{1.24}$$

A single pulse is π/δ long. In case of a constant Rabi-frequency the system is fully transfered to the excited state when $\Omega t = \pi$. The left term is replaced by the time-integral over the Rabi-frequency envelope which results in the so-called π-pulse condition

$$\Omega_0 = \frac{\pi\delta}{4} \tag{1.25}$$

where Ω_0 is the Rabi frequency of one of the initial beams. The right side can be replaced by odd multiples, since any number of full and one half precessions yield the final excited state. Assuming that a right propagating pulse excites the system by absorption, a successive pulse from the left propagating beam causes stimulated emission and transfers the system back to the ground state, $\Delta p = 2\hbar k$ of momentum are transfered onto the atom. Multiple processes yield a force $F_{bichro} = \frac{2\hbar k\delta}{\pi}$.

If spontaneous emission occurs, the atom will be in the ground state again and the sign of the forces is reversed. The force for multiple processes averages to zero. A non-vanishing force can be achieved if the second pulse arrives after a quarter of the first pulse. The possibility that a decay occurs at the wrong time is now 1/4, whereas the restoring decay happens with probability 3/4.

The two possibilities add up to the resulting force

$$F_{Bichro} = \left(\frac{3}{4} - \frac{1}{4}\right)\frac{2\hbar k\delta}{\pi} = \frac{\hbar k\delta}{\pi}. \tag{1.26}$$

The force becomes, for detunings much greater than the decay rate $\delta \gg \gamma$, considerably larger than the radiative force. Increasing δ to yield larger forces, also requires higher Rabi frequencies to keep the π-pulse condition satisfied. Therefore the force can not be made arbitrarily large. At high enough intensities nonlinear effects are going to contribute and the previous assumptions will no longer be valid.

The bichromatic processes can also be discussed in the dressed atom picture, then called the doubly dressed picture [18, 19]. Two frequencies results in an infinite number of levels spaced by δ. Where next levels are coupled alternately by the two detuned radiation fields, described by their Rabi-frequencies $\Omega_{1,2}$. In case of a non-zero phase between the two modes, the spatial dependence of the Rabi frequencies results in the variation of the dressed Eigenenergies within one wavelength. Level crossings via Landau-Zener transitions occur.

Both pictures neglect effects from detuning and neglect decay or treat it in a simplified way. For a more quantitative prediction of the force under realistic conditions numerical calculations can be done. These yield a force of approximately 3/4 of the prediction of the π-pulse model.

The bichromatic force has so far been investigated for Sodium [16], Rubidium [3, 20], Cesium [21] and Helium [2, 22, 23]. It has been shown that the optical forces achievable are not limited by the lifetime of the transition. The

capture range is greater than that of the radiative force. The results found were in agreement with the numerical predictions. Today it is used in our lab to collimate an intense atomic beam for neutral atom lithography [24]. This allows us exposure times below one hour rather than several hours.

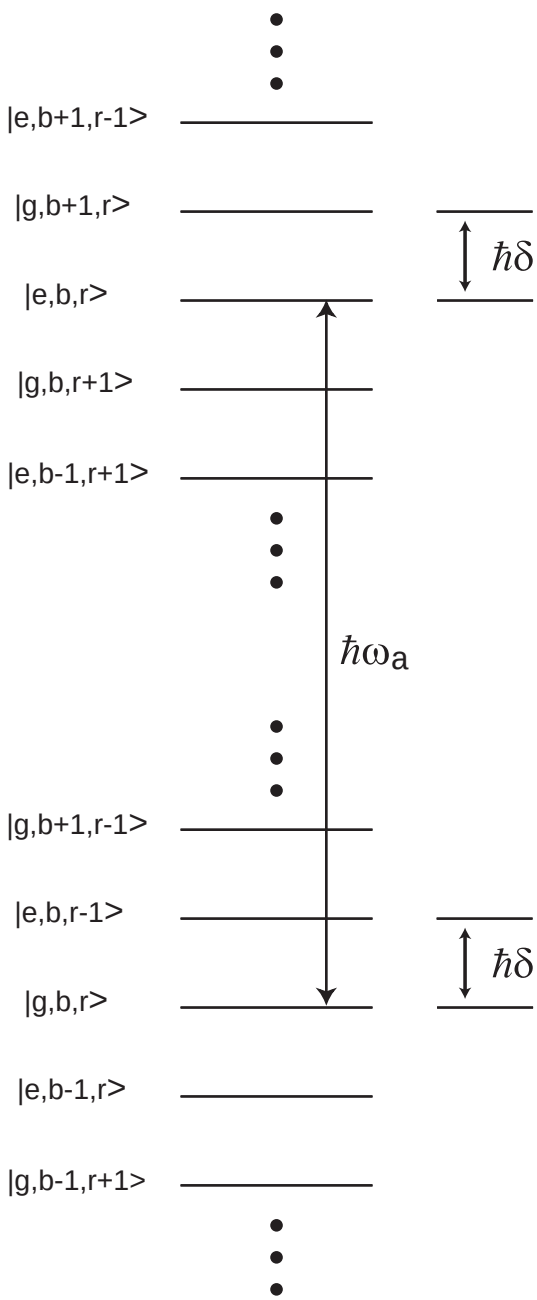

Figure 1.9: The presence of two radiation fields which are oppositely detuned by $\delta/2$ from the atomic resonance, results in an infinite number of dressed energies spaced by δ. Figure out of [15].

1.4 Properties of Helium

This experiment uses metastable 2^3S_1 Helium (He^*). The decay into the absolute ground state 1^1S_0 is doubly forbidden by the selection rules $\Delta L = \pm 1$ and $\Delta S = 0$. The lifetime of the 2S state is $\tau \approx 8000\,\mathrm{s}$, large enough that it can be considered to be stable for the time the atoms are in the experiment. It was measured recently in [25]. These metastables carry almost 20 eV of energy, which makes them easy to detect and useful for lithography. Our two-level system uses the transition $2^3S_1 \rightarrow 2^3P_2$, whose wavelength is $\lambda = 1083\,\mathrm{nm}$ with width $\gamma = 1/\tau = 2\pi \times 1.62\,\mathrm{MHz}$. These and other properties are summarized in table 1.1. ^{4}He has no hyper fine structure, due to the fact that the nuclear spin is zero.

	λ [nm]	$\hbar\omega_a$ [eV]	τ [ns]	$\gamma/2\pi$ [MHz]	I_{sat} [mW/cm^2]	v_r [cm/s]
$2^3S_1 \rightarrow 2^3P_2$	1083.331	1.14	98.04	1.62	0.17	9.8
$2^3S_1 \rightarrow 1^1S_0$	62.6	19.82	8×10^{12}	-	-	-

Table 1.1: Properties of the 2-level system and the forbidden transition to the ground state. The information was taken out of [14].

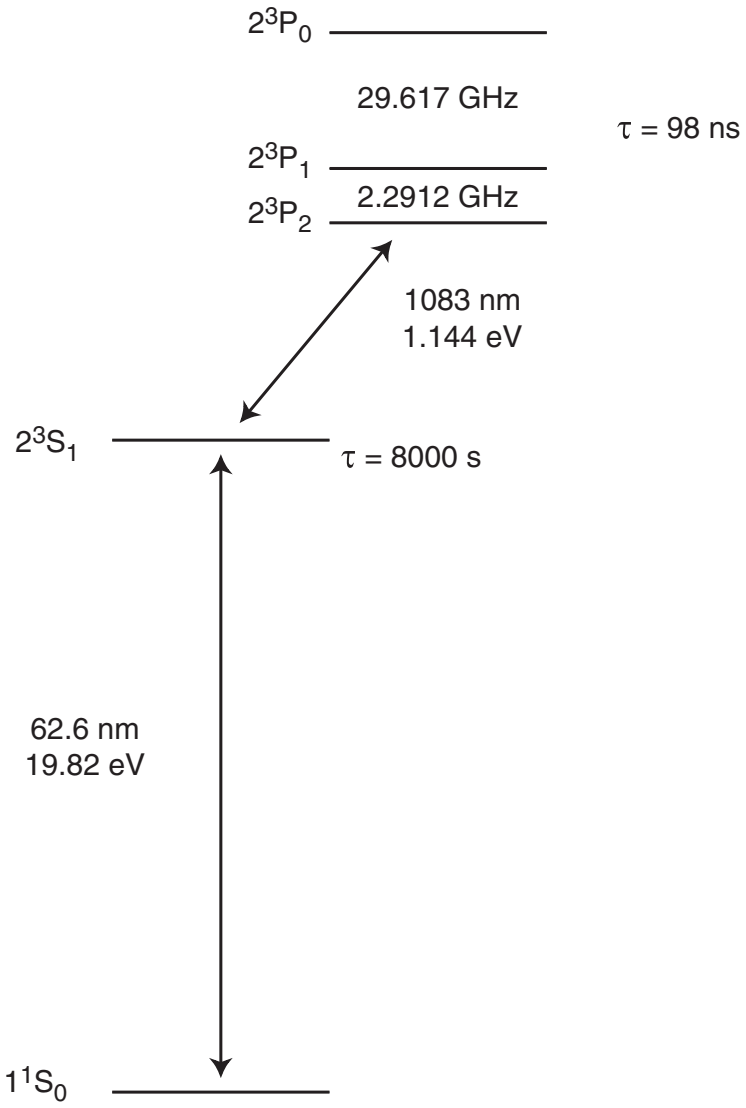

Figure 1.10: Simplified scheme of all energies of Helium relevant to our experiment [5].

Chapter 2

Theory of Adiabatic Rapid Passage Sequences

The population inversion of a two-level system by adiabatic rapid passage (ARP) has been known in nuclear magnetic resonance for a long time [26]. It requires the torque vector $\vec{\Omega}$ to be swept from one pole of the Bloch sphere to the opposite one, slowly enough that the Bloch vector $\vec{R}$ is able to adiabatically follow and fast enough such that relaxation can be neglected. In the case of an optical two level system a light pulse is needed whose frequency is swept through resonance [27, 28]. The length of the pulse has to be short compared the life time of the transition. Pulse sequences of two counter-propagating beams can drive the system coherently between ground and excited state and exert forces larger than the radiative force $F_{rad} = \hbar k\gamma/2$, since this scheme does not depend on spontaneous decay. The theory presented here is mostly taken out of [5].

2.1 Adiabatic Rapid Passage

An adiabatic rapid passage can be performed by a chirped, optical light-pulse. The optical frequency is swept through the resonance of the transition, while the amplitude-envelope forms a symmetric pulse, reaching its maximum at resonance.

An ARP process is most easily explained in the adiabatic frame, either in the dressed atom or the Bloch sphere picture. The Hamiltonian in the adiabatic frame, describing our system is

$$\mathcal{H} = \frac{\hbar}{2} \begin{pmatrix} -\delta(t) & \Omega(t) \\ \Omega(t) & \delta(t) \end{pmatrix}, \tag{2.1}$$

where the detuning and the Rabi-frequency are constantly changing. This Hamiltonian yields the eigenenergies $E_{1,2} = \pm\frac{\hbar}{2}\sqrt{\delta^2 + \Omega^2}$. The trajectory of the atomic state can be followed in a 3D dressed picture (Fig. 2.1). The new eigenstate, corresponding to this eigenenergy, transforms from the original ground state $|g\rangle$ in case of positive detuning $\delta(t) > 0$, through a mixed state for $\Omega(t) \neq 0$ and to the original excited state $|e\rangle$ for $\delta(t) < 0$ [29, 30]. The same is true if it starts in in the excited state on the upper energy sheet.

For a slow enough sweep of amplitude and frequency, the two level system follows the adiabatic state, resulting in a population inversion. If spontaneous emission is considered, it is obvious that a pulse has to be significantly shorter than the lifetime of the two level system, or in other words the sweep-frequency has to be considerably larger than the decay rate $\gamma \ll \omega_m$. Hence the name **A**diabatic **R**apid **P**assage.

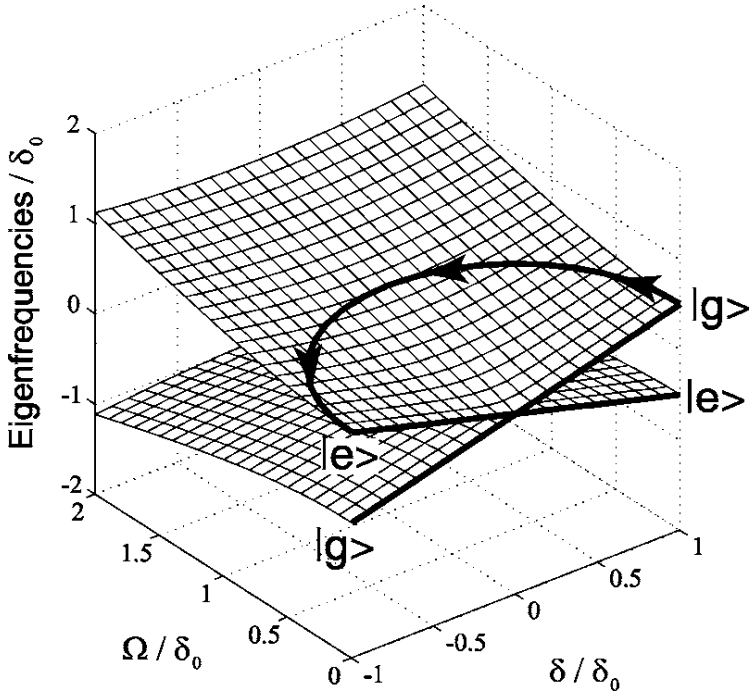

Figure 2.1: Following the trajectory of the dressed energies. The corresponding eigenstate is for $\Omega_0 \neq 0$ a mixture of the original eigenstates. Taken out of [30].

Another useful way of looking at it is the Bloch sphere picture described in Sec. 1.1.3. The motion of the Bloch vector is described by Eq.(1.17). For a constant torque the Bloch vector precesses around the torque. If the torque is swept, the Bloch vector tries to stay on the same orbit, therefore keeping its distance and following the torque, if the sweep is slow enough. Sweeping the Bloch vector from the south to the north pole leads to a population inversion. The proximity of the Bloch vector to the torque can be observed in Fig. 2.2. The adiabaticity of the sweeping is quantified by the condition

$$\left|\vec{\Omega}(t)\right| \gg \frac{\mathrm{d}\theta}{\mathrm{d}t}, \tag{2.2}$$

where $\theta(t) = \arctan\big(\delta(t)/\Omega(t)\big)$ is the angle between the r_3-axis and the torque vector $\vec{\Omega(t)}$. It is also the mixing angle of the adiabatic state in the dressed picture. The condition reads that the angular frequency of the torque vector must be small compared to the angular frequency of the Bloch vector at all times.

ARP has contradicting requirements: Eq. (2.2) and the fact that we have to sweep fast enough that spontaneous decay can be neglected. It is therefore possible that a sweep is not perfectly adiabatic. As a result some fraction of the population is going to remain in the ground state; their transitions were non-adiabatic. The so called non-adiabatic transition probability P_{nad} has to be small for efficient momentum transfer.

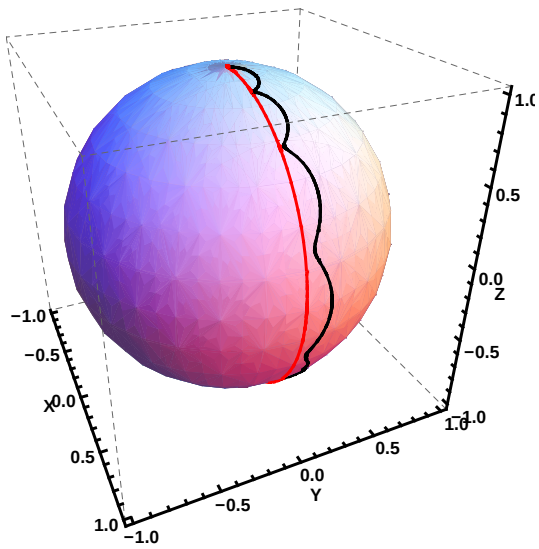

Figure 2.2: The Bloch vector(black) follows the torque(red). If the transition is adiabatic the population is inverted. This trajectory was calculated numerically for the parameters $\Omega_0 = 12.1\,\omega_m$ and $\delta_0 = 16\,\omega_m$. The parameters will be explained in Sec. 2.2.

2.2 Non-adiabatic Transition Probability

The non-adiabatic transition probability P_{nad} is clearly dependent on the Rabi-frequency $\Omega(t)$ and detuning $\delta(t)$. To characterize this dependence a model for a swept pulse is required. There are various common models in literature used to study the adiabatic passage. The Rabi-frequency is described by a rectangular, triangular, sinusoidal, Gaussian, Lorentzian or $1/\cosh$ pulse, and the detuning by a linear, cosinusoidal or tanh function. A detailed comparison of these can be found either in [31] or [5]. For the purposes of our calculations sinusoidal pulses for the Rabi frequency are used because they are finite, and cosinusoidal detuning because they are experimental reality

$$\Omega(t) = \Omega_0 \sin \omega_m t \tag{2.3a}$$

$$\delta(t) = -\delta_0 \cos \omega_m t \tag{2.3b}$$

where ω_m is the modulation frequency and $t \in \left[0, \pi/\omega_m\right]$. These assumptions allow us to characterize P_{nad} in terms of the Rabi-frequency peak value Ω_0 and the detuning amplitude δ_0.

Assuming that we are in the ground state at $t = 0$, we define P_{nad} as the probability that we remain there after a single pulse, which can be written as

$$P_{nad} = \rho_{gg} = \frac{1 - r_3(\pi/\omega_m)}{2}. \tag{2.4}$$

The component r_3 can be calculated by integrating the Eq. (1.17) from $t = 0$ to $t = \pi/\omega_m$. There is no analytic solution for arbitrarily chosen parameters δ_0 and Ω_0. Special cases like $\delta_0 = \Omega_0$ [32] or $\delta_0 = 0$, which is just a π-pulse

for the right Ω_0, are solvable and have been studied. Arbitrary parameters require numerical integration which is not limited to these special cases. The initial Bloch vector is set to $\vec{R} = (0, 0, -1)^\intercal$, δ_0 and Ω_0 are expressed in terms of the sweep frequency ω_m and the equations are evaluated until $t = \pi/\omega_m$. Retrieving r_3 and calculating P_{nad} is trivial. Technical details of the integration are discussed in Ch. 3; a sample code can be found in the appendix.

Doing the numerical integration yields the maps shown in Fig. 2.3. The analytic case of $\Omega_0 = \delta_0$ can be found on the diagonal and the solution is confirmed. Note the periodicity at the left edge $\delta_0 = 0$ of the map: P_{nad} is minimal for Ω_0/ω_m equal to odd multiples of $\frac{\pi}{2}$, as the π-pulse condition Eq. (1.25) predicts and maximal at multiples of π. This map is symmetric for negative δ_0 and Ω_0. The part shown can be unfolded by mirroring it subsequently on both axes.

Looking at the logarithmic map, the position of the minima can be followed for $\delta_0 \neq 0$. For small sweeping amplitudes δ_0 and with the exception of the first minima at $\Omega_0 = \frac{\pi}{2}\omega_m$, the trajectory of all the other minima is bent towards smaller Ω_0 for increasing δ_0, approximately following a circle around the origin. This indicates that the π-pulse condition is still met for the generalized Rabi frequency $\Omega' = \left|\vec{\Omega}\right|$. Large δ_0 results in a different behavior; starting with the first ($\Omega_0 = \frac{\pi}{2}\omega_m$) minima at $\delta_0 = 0$, every other pairs up with the next higher one, since the trajectories of their minima join.

2.3 Periodicity

Upon looking at some point in the parameter space, preferably close but not on some minima of P_{nad}, integrating Eq. 1.17 for many periods, we will see that the trajectory of the Bloch-vector is contained within bands, as shown in Fig. 2.4. This periodicity can also be observed if we are plotting only one point after each period/sequence. These are found to lie on a circles, which go through the pole as shown in Fig. 2.5. Interestingly, the circles switch side depending on whether they are outside or inside the minima loop of P_{nad}.

Let us first consider a single pulse, that drives the Bloch-vector, from the initial state $\vec{R}(t) = (0, 0, -1)^\intercal$, close to the north-pole. A second pulse, regardless from what direction it is coming, lets the evolution of the vector continue and and the trajectory of $\vec{R}$ ends close to the south-pole. The fact that $\vec{R}(2\pi/\omega_m)$ is close to the south pole does not mean that $\vec{R}(\pi/\omega_m)$ was close to the north-pole, although the reverse is true. It has been shown by [30] that the time-evolution $t = 0 \rightarrow 2\pi/\omega_m = T_m$ of the Bloch-vector under the influence of the torque $\vec{\Omega}$ can be written as a rotation

$$\vec{R}(T_m) = \mathcal{U}(T_m)\vec{R}(0), \tag{2.5}$$

where $\mathcal{U}(T_m)$ is dependent on the evolution of the torque $\vec{\Omega}(t)$. Instead of looking at it as a rotation of the Bloch-vector, it can be equivalently understood as a rotation of the Bloch-sphere. This makes the evolution independent of the current position of $\vec{R}(t)$. It is also possible to define $\mathcal{U}(t)$ for arbitrary t, which is going to be used in the following chapter. For now, we are only

interested in the position of $\vec{R}$ after each each complete cycle.

The rotation matrix $\mathcal{U}(T_m)$ is given by three parameters, two angles (θ_a, φ_a) defining the rotation axis and one being the rotation angle α. Repetitive rotations of the initial state, yield the points $\vec{R}(nT_m)$, which all lay on a circle whose center is the rotation axis and that does go through the south-pole. Its radius r_0 is the distance between the axis and the south-pole. Successive $\vec{R}(nT_m)$s are separated by the angle α. The proximity of $\vec{R}(T_m)$ to the south pole does not indicate that the axis is close to it, thus the radius r_0 is not necessarily small. It shall also be mentioned that the points $\vec{R}\big((n{+}1/2)T_m\big)$ are located on a similar circle at the north pole. This agrees with the confinement of the trajectories within bands.

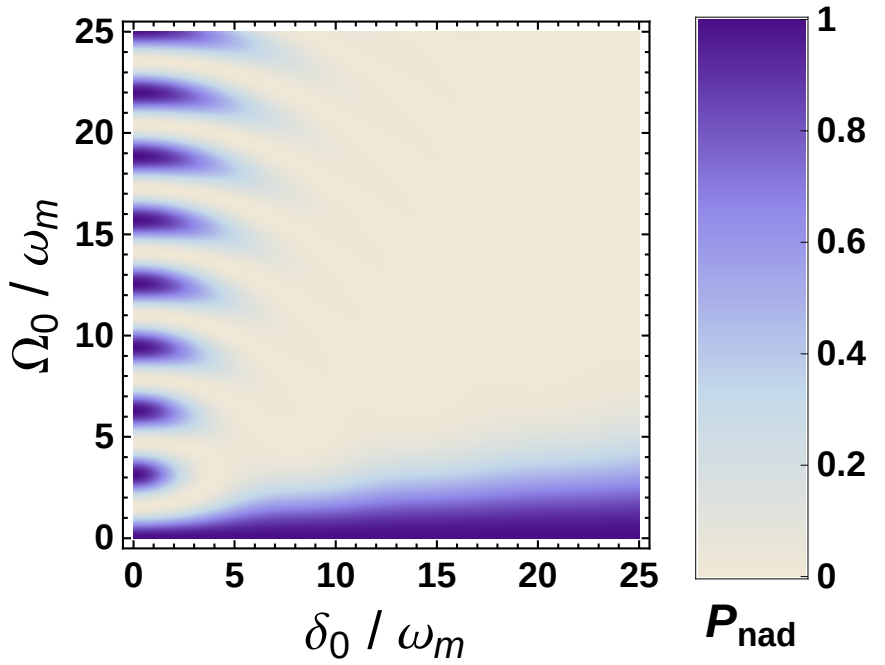

(a) linear scale

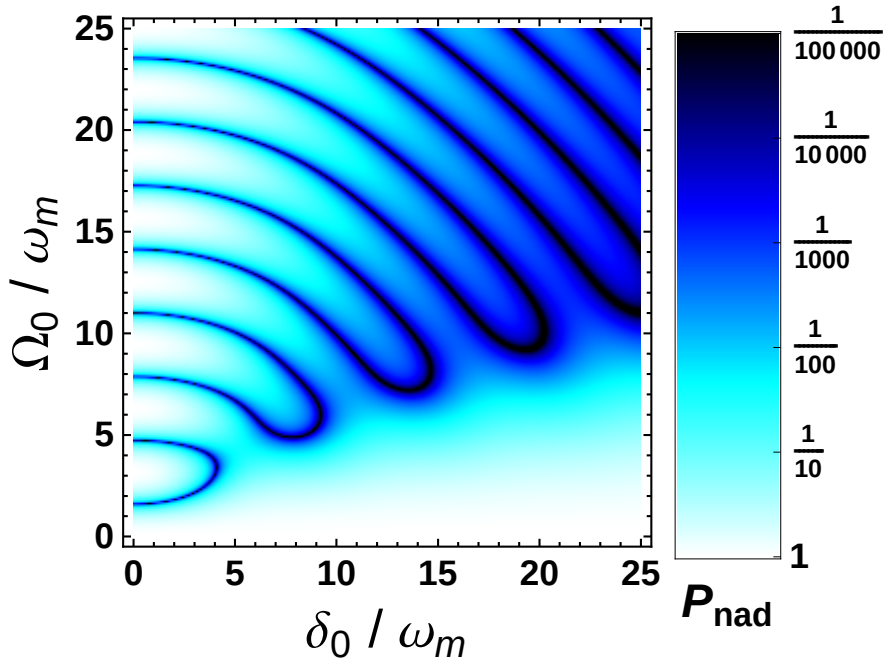

(b) logarithmic scale

Figure 2.3: Map of the non-adiabatic transition probability P_{nad}.

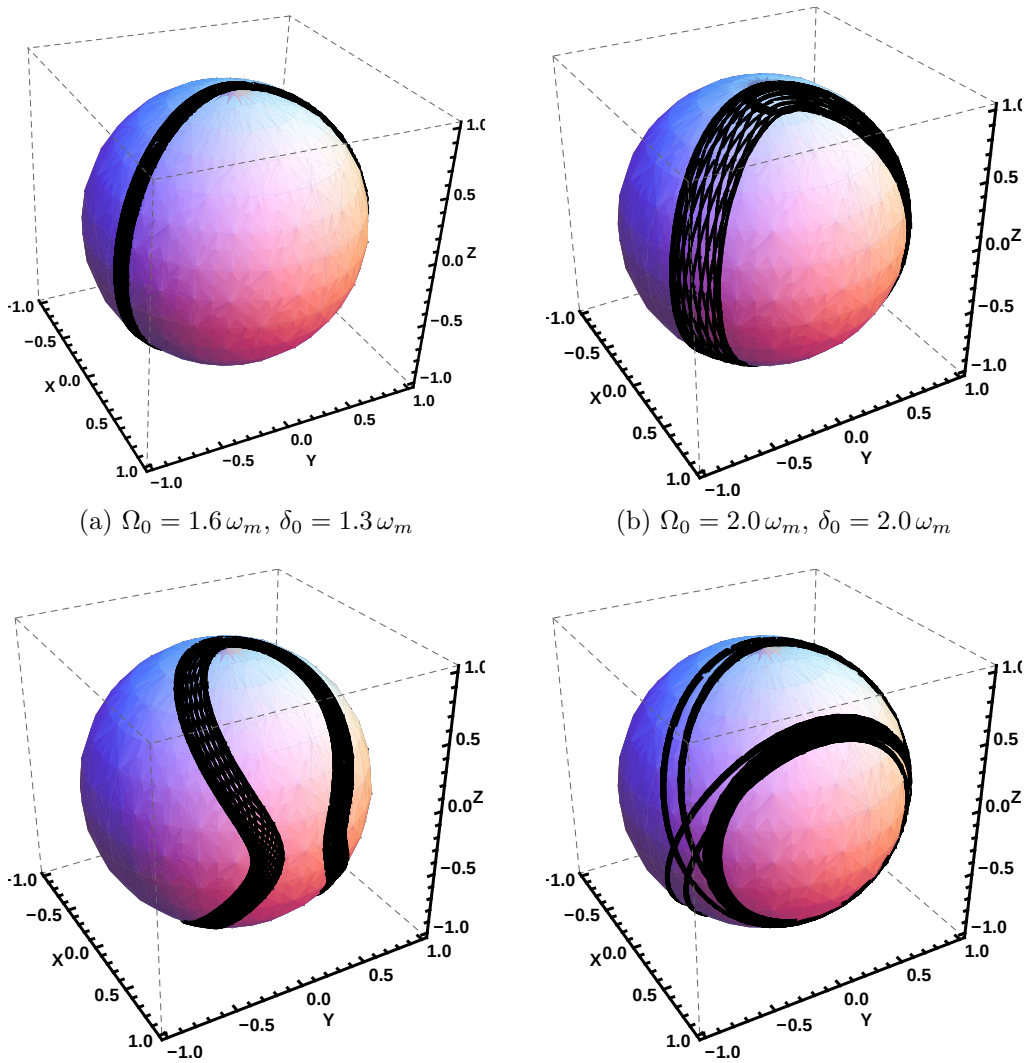

(a) $\Omega_0 = 1.6\,\omega_m$, $\delta_0 = 1.3\,\omega_m$

(b) $\Omega_0 = 2.0\,\omega_m$, $\delta_0 = 2.0\,\omega_m$

(c) $\Omega_0 = 2.9\,\omega_m$, $\delta_0 = 3.7\,\omega_m$

(d) $\Omega_0 = 4.5\,\omega_m$, $\delta_0 = 1.9\,\omega_m$

Figure 2.4: Plots of trajectories on the Bloch sphere for various parameters.

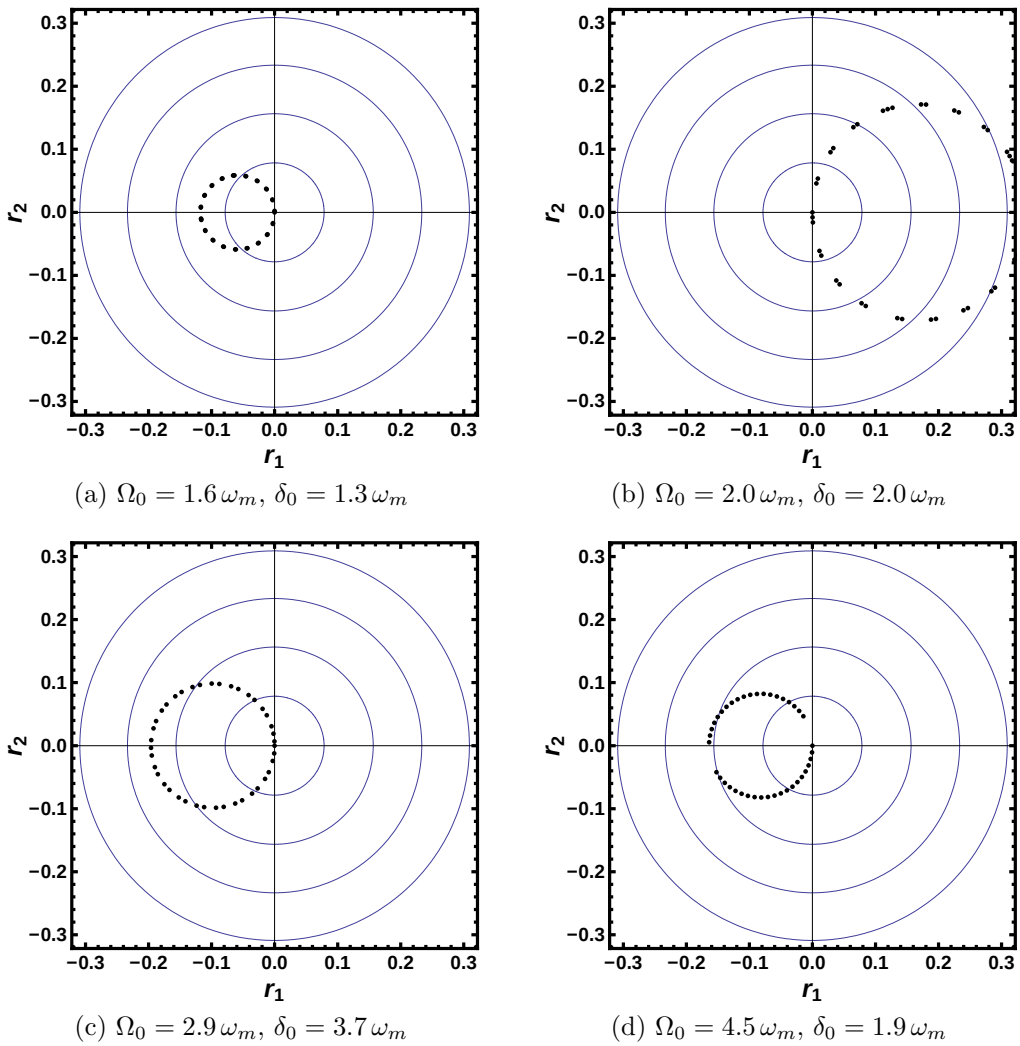

(a) $\Omega_0 = 1.6\,\omega_m$, $\delta_0 = 1.3\,\omega_m$

(b) $\Omega_0 = 2.0\,\omega_m$, $\delta_0 = 2.0\,\omega_m$

(c) $\Omega_0 = 2.9\,\omega_m$, $\delta_0 = 3.7\,\omega_m$

(d) $\Omega_0 = 4.5\,\omega_m$, $\delta_0 = 1.9\,\omega_m$

Figure 2.5: This is the view looking up at the southpole. In similarity to Poincare surfaces points after each cycle (consisting of two pulses) are plotted, since the time evolution for one cycle can be interpreted as the rotation of the Bloch sphere. Multiple rotations lead to the observed circles, whose center is the axis the Bloch sphere is rotated around.

2.4 Force from Periodic ARP Sequences

After showing that multiple ARP sequences exhibit periodic behavior on the Bloch sphere, which is a requirement for a stable force, I now want to derive the quantitative behavior of the force. The force onto the atom can be calculated using the Ehrenfest theorem [14]

$$\vec{F} = < -\vec{\nabla}\mathcal{H} > = \mathrm{Tr}\big[\,\vec{\nabla}\mathcal{H}\rho\,\big] = \frac{\hbar}{2}\big(r_1\vec{\nabla}\Omega_1 + r_2\vec{\nabla}\Omega_2\big), \tag{2.6}$$

where Ω_i and r_i are the corresponding components of torque and Bloch vector. In case of two counter-propagating light fields whose wavenumber is k the derivative yields

$$\vec{F} = \frac{\hbar\vec{k}}{2}\left(\big(\vec{\Omega}_+ - \vec{\Omega}_-\big) \times \vec{R}\right)_3 \tag{2.7}$$

where the force is given by the third component of this vector product. The torques $\vec{\Omega}_+$ and $\vec{\Omega}_-$ belong to the right and left propagating fields. In case of temporal overlapping additional effects such as multi photon processes have to be considered [33]. If the pulse are not temporally overlapped we can treat them individually and write

$$\vec{F} = \pm\frac{\hbar\vec{k}}{2}\left(\vec{\Omega}_\pm \times \vec{R}\right)_3 = \pm\frac{\hbar\vec{k}}{2}\dot{r}_3. \tag{2.8}$$

Identifying $\dot{r}_3$ yields an expected result: a momentum of $\hbar k$ is exchanged if the Bloch vector is driven from one pole to the other. The force of a single

pulse expressed through discretization of $\dot{r}_3$ is

$$\bar{F} = \pm\frac{\hbar k}{2}\frac{\omega_m}{\pi}\Delta r_3 = \pm\frac{\hbar k \omega_m}{\pi}\big(1 - P_{nad}\big) \tag{2.9}$$

where π/ω_m is the length of the pulse.

The phase of the Rabi frequency is dependent on the relative position of the individual atom, since $\tilde{\mathcal{H}}_{eg} = \hbar\Omega\exp\big(-\mathrm{i}(kz - \omega t)\big)$. The position dependent, relative phase between right and left- propagating pulse changes by a full period 2π over half a wavelength. This is clearly smaller then the spread of the atomic ensemble in our experiment. To account for that, the force is averaged over every possible phase. The derivation, which can be found in appendix B of [5], yields

$$\bar{F} = \pm\frac{\hbar k \omega_m}{\pi}\left(1 - \sqrt{P_{nad}}\right) \tag{2.10}$$

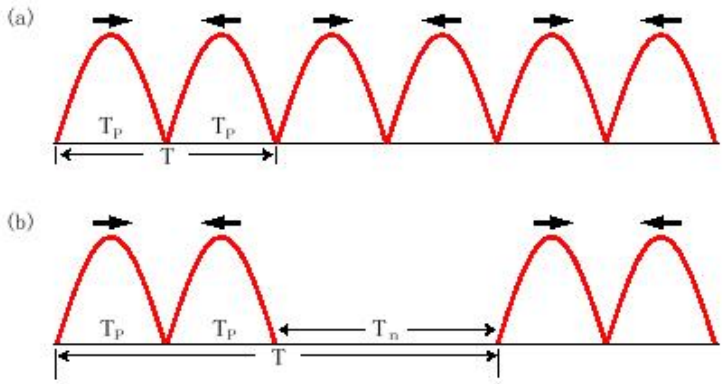

Figure 2.6: Pulse scheme that breaks the left/right symmetry. The force gains directionality, the atom is now more likely to be pushed to the left. Figure taken out of [12].

So far spontaneous emission has been neglected. A similar approximation as in the case of the bichromatic force (Sec. 1.3) can be made. If spontaneous decay occurs during the time π/ω_m of a exciting pulse, the force is reversed. Multiple such processes average our force to zero. We are introducing a syncopation time $2\pi/\omega_m$, after the counter-propagating pulse, with no field present. This is shown in Fig. 2.6. The probability that a decay is restoring the right direction becomes $\frac{3}{4}$. The effective ARP-force is

$$F_{ARP} = \frac{\hbar k}{T}(1 - \sqrt{P_{nad}}) \tag{2.11}$$

where $T = 4\pi/\omega_m$ is the length of the complete pulse sequence. This however does not take possible Doppler-detuning into account and treats spontaneous decay naively.

Chapter 3

Numerical Simulations

The numerical integration of the Optical Bloch Equations (1.17) yield the trajectory of the Bloch-Vector for a given pulse sequence. This pulse sequence is described by the time-dependent torque vector $\vec{\Omega}(t)$. The extraction of the the non-adiabatic transition probability is obvious; the force can be calculated using Eq. (2.8). The control of the torque allows one to model imperfections of the experiment as well as look at purely theoretical aspects of ARP.

Numerical simulations where done on two platforms: in `Mathematica` and `c++` using the gnu scientific library (gsl)[1]. A sample of both codes can be found in the appendix. Both environments allow us to choose between a selection of integration methods. Different methods yielded comparable performance; no major differences were found. Subsequently an 8th order Runge-Kutta algorithm was used. The parameters used during these calculations resemble resemble our experimental situation.

[1] http://www.gnu.org/software/gsl

3.1 Effects of Spontaneous Emission

For large momentum transfers the sequences have to be repeated many times. On these time scales spontaneous emission can not be neglected and has to be included. This can be done by a simple estimate like in Sec. 2.4, or be directly included into the numerical integration. This has been done using two different methods: by a modification of the Optical Bloch Equations or by using a Monte-Carlo approach. The decay rate throughout all calculations has been set to $\gamma = \omega_m/100$.

The optical Bloch equations are modified according to [14]. The decay of r_1, r_2 and r_3 can be described by the same rate, since we assume that spontaneous emission is the only possible decay channel. If collision and other decay channels are considered, additional parameters are required. Including the decay rate γ into the differential equations for the elements of the density matrix and deriving the time-dependence of the individual components leads to the modified optical Bloch equations

$$\dot{\vec{R}} = \vec{\Omega} \times \vec{R} - \gamma \begin{pmatrix} r_1/2 \\ r_2/2 \\ r_3 + 1 \end{pmatrix}. \tag{3.1}$$

Note that with the additional term the Bloch-vector will no longer stay nor-

malized, since

$$\frac{\mathrm{d}}{\mathrm{d}t}\vec{R}^2 = 2\vec{R}\cdot\dot{\vec{R}} = -2\gamma\,\vec{R}\cdot\begin{pmatrix} r_1/2 \\ r_2/2 \\ r_3+1 \end{pmatrix} = -2\gamma\big(r_1^2/2 + r_2^2/2 + r_3^2 + r_3\big) \quad (3.2)$$

is only zero for the special case that the system is in the ground state $\vec{R} = (0, 0, -1)^\intercal$. The decay of R is correct; one occasion where it is expected to happen is the case of a constant Rabi-frequency (and no detuning) in which the Bloch oscillations are damped until the system is an superposition of ground and excited state, with random phase (averaging out to zero). It does not, however, result in a vanishing Bloch vector for an arbitrary pulse sequence (for either up-down and up-up), as can be seen in Fig. 3.1. The decay of the Bloch-vectors length $|\vec{R}|$ is interrupted and reversed, because Eq. (3.2) can also be positive. This is the case when $r_1, r_2 \simeq 0$ are comparably small and r_3 is negative and not equal to -1. Note that without syncopation time, $|\vec{R}|$ would vanish. The length of the Bloch vector decays until it equilibrates and continuous to irregularly oscillate about an average length. This length depends on the parameters δ_0, Ω_0, and can be correlated to P_{nad}.

The second method used was to run optical Bloch equations code without the additional term. Decay was realized by restoring the ground-state with the probability $p = \gamma\frac{r_3+1}{2}\mathrm{d}t$ after each step $\mathrm{d}t = \frac{T_c}{1000}$, using random number generation[2]. This was done in `c++`, which allows one to access and manipulate all variables at any time. Averaging over a large number of trajectories the

[2]Algorithm by R. M. Ziff

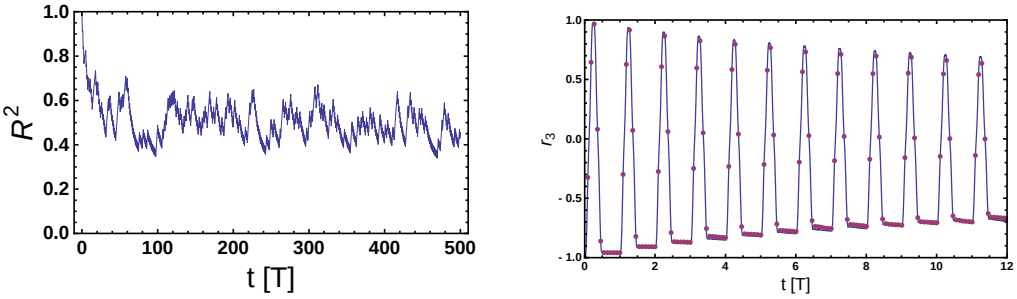

(a) Time dependence of $\vec{R}^2$

(b) Time dependence of r_3

Figure 3.1: a) Time dependence of $\vec{R}^2$ for a timescale comparable to the experimental interaction time. b) Comparison of the direct integration of Eq. (3.1) (blue) and the average over 1000 Monte Carlo trajectories (purple).

previous method can be confirmed (Fig. 3.1). An approximate force map is calculated by retrieving P_{nad} from the integration of Eq. (3.1) and using Eq. (2.11) to calculate the force. This is shown in Fig. 3.2.

The modeling of the experiment includes spontaneous emission, since our total interaction time T_{int} is approximately a few lifetimes of the excited state. Depending on the point in the parameter space of ARP, meaning δ_0 and Ω_0, even the relaxation time might be non-negligible and will yield additional effects.

3.1.1 Force Distribution

Rather than averaging over all trajectories, the Monte-Carlo approach can be used in a different way. Following many single trajectories, a distribution of the accumulated momentum exchange can be retrieved, for any sweeping scheme and parameters δ_0 and Ω_0. This corresponds to a force distribution. This is shown in Fig. 3.3.

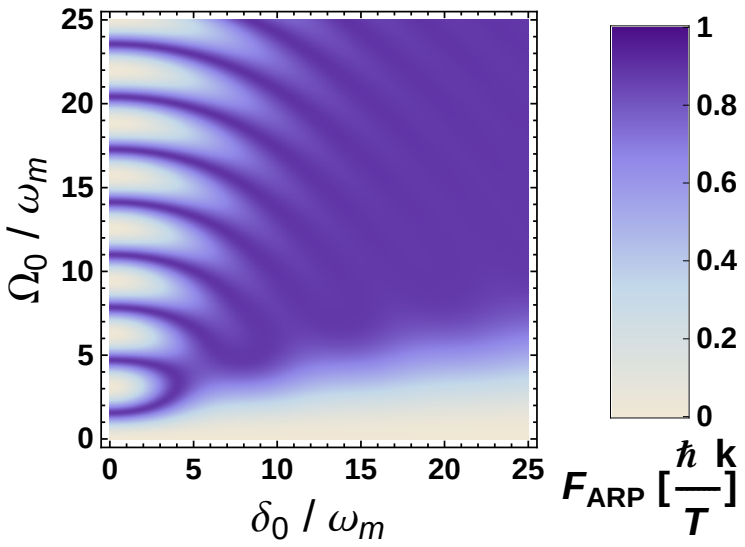

Figure 3.2: A approximate force map. The force is expressed in momentum kick $\hbar k$ per cycle time T. This force map corresponds to the approximate force maps shown in [5] except for a constant factor κ.

The deconvolution of the experiment becomes even more difficult since the deflection is given by integrating over the varying interaction time and the force distribution.

3.2 Velocity dependence

Moving atoms see Doppler-detuned frequencies. The velocity dependence is included by shifting the detuning $\delta(t)$ of the counter-propagating pulses by $\vec{k} \cdot \vec{v} = kv$ in opposite directions, where k is the wavenumber of the light and v the transverse velocity. Their product kv is either expressed in units of the sweep frequency ω_m or the decay rate γ. Force-profiles like Fig. 3.4 are calculated showing the velocity dependence.

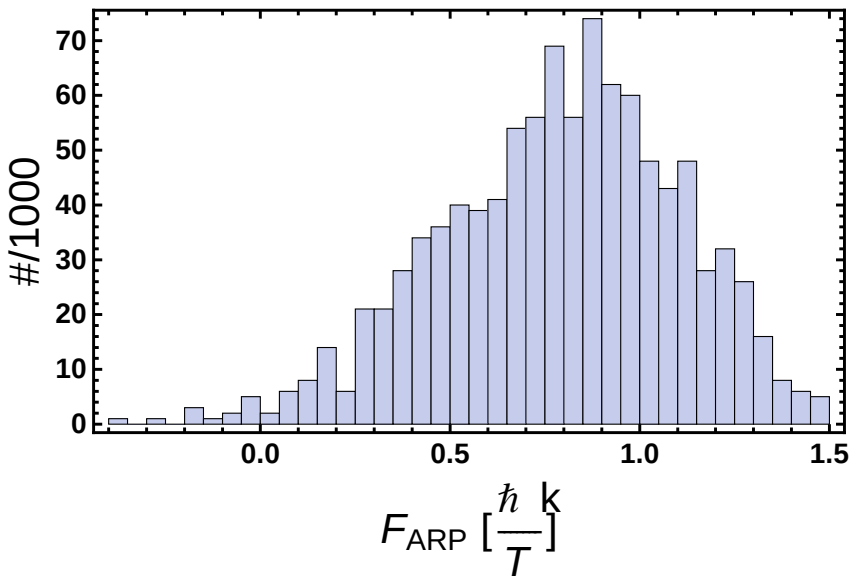

Figure 3.3: Force distribution for a sample of 1000 trajectories at $\Omega_0 = 2.4\,\omega_m$, $\delta_0 = 1.8\,\omega_m$ and alternating sweep directions. The integration time was 240 cycles such that system experienced on average 6 decays. The mean force is $\bar{F} = 0.79\,\hbar\mathrm{k}/\mathrm{T}$ and the width is $0.25\,\hbar\mathrm{k}/\mathrm{T}$.

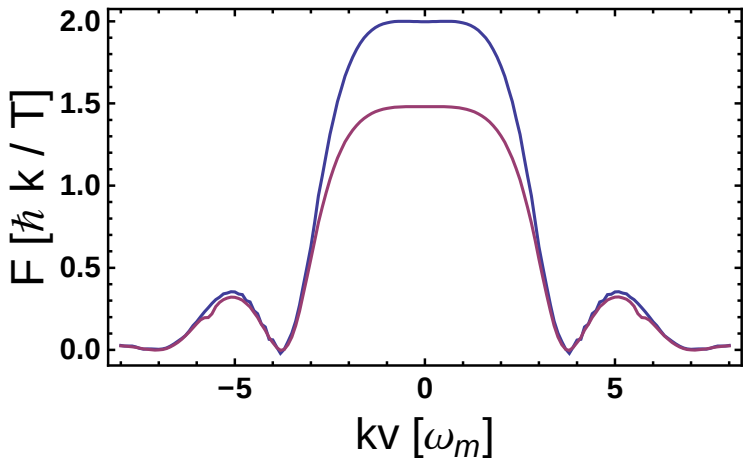

Figure 3.4: Force-profiles calculated by the integration of Eqs. (1.17 or 3.1) showing the velocity dependence of the ARP force at $\Omega_0 = 3.45\,\omega_m$, $\delta_0 = 4.25\,\omega_m$ and up-down sweeping. The blue line neglects spontaneous decay, the purple one included spontaneous decay according to Eq. (3.1). A limited integration time of 20 cycles was not sufficient for the equilibration of $|\vec{R}|$, such that the strength of the force in this plot is still strongly influenced by the first cycles. The approximate capture range for this set of parameters is $6\omega_m$.

3.2.1 Capture range

Mapping the parameter space, force profiles for $\delta_0 \in [0, 5\,\omega_m]$ and $\Omega_0 \in [0, 5\,\omega_m]$ in steps of $0.1\,\omega_m$ where obtained. The calculation included spontaneous emission and was done using up-down pulse-sequences which will be discussed in the next section. The integration time was 40 cycles. We define the capture range as the full width at half maximum(FWHM) of the force. Since the force profiles are complicated and may have their maximum at a different velocity than zero, it is sometimes not possible to define a capture range. In these cases, defined by the fact that the force at zero velocity was not within the FWHM of the the maximum force, the capture range was set to zero. The resulting capture range map and a force map out of the same

calculations are shown in Fig. 3.5.

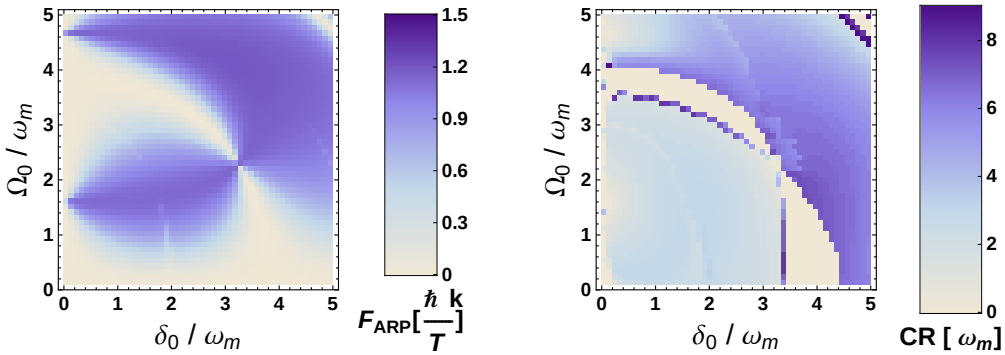

(a) Force map

(b) Capture range map

Figure 3.5: ARP capture range (CR) in units of ω_m. Note the areas where we could not define a capture range and set it to zero. The shallow features are effects of spontaneous decay and disappear as soon as it is neglected. Note that a big CR does not necessarily mean that the force is big itself.

3.3 Sweep direction

Looking at Fig. 3.5 the reader might be confused by the shown force-map whose structure does not corresponds to previously shown maps. This is explained in this section. Demonstrations of optical force via ARP have so far been made in setups using retro-reflected beams. Inherent to this setup is that every pulse is swept up. Using two individual beams to measure the velocity capture range adds the possibility to explore alternating sweep directions. These have been modeled.

Choosing a parameter ($\Omega_0 = 3.45\,\omega_m$, $\delta_0 = 4.25\,\omega_m$) set which has a small non-adiabatic transition probability, force profiles for up-down and up-up sequence were calculated and are shown in Fig. 3.6. This shows a rather large

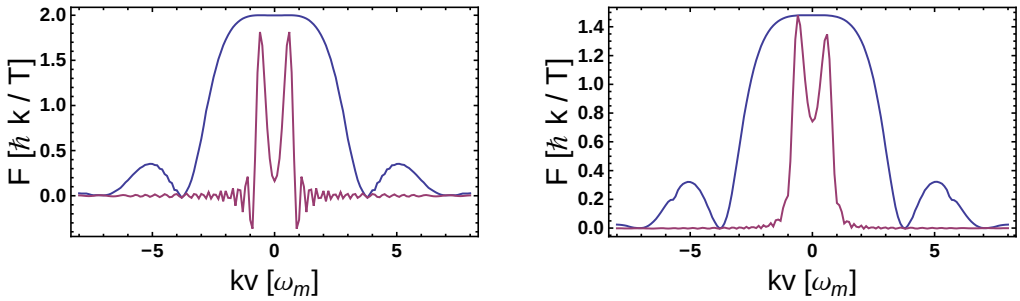

(a) neglecting decay (b) including decay

Figure 3.6: Force profiles for the parameters $\Omega_0 = 3.45\,\omega_m$ and $\delta_0 = 4.25\,\omega_m$. The integration time was 20 cycles and the decay rate $\gamma = \omega_m/100$. The small oscillations in a) vanish for a longer integration time. The blue line is for up-down and the purple line for up-up sweeps.

capture range for up-down, sequences compared to up-up sequences. Also note the asymmetry of the up-up force profile. This feature occurs as soon as spontaneous emission is included into the calculation. It is confirmed in Monte-Carlo simulations such that numerical errors can be excluded. Future work is intended.

The stability of up-down can again be explained by rotations of the Bloch-sphere. The effect of pulse sequences can be described as a rotation of the Bloch-sphere as discussed in Sec. 2.3. The same is also true for single pulses. Assuming that P_{nad} is close to but not zero, one pulse will rotate the Bloch-vector close to the north pole. Single up and down pulses do have the same P_{nad}, the only difference between them is, that they are going up on opposite sides since their detunings have alternate signs. More precisely their trajectories are symmetric about the r_1r_3-plane, which means the only difference between their end points is that they have opposite r_1-values. Doing the same transformation two or more times results in a greater distance to the desired

pole, which results in instabilities in case of up-up sequences. Up-down sequences, on the other hand, do not cross over the north pole to get back down again. They go back on a somewhat similar trajectory, which compensates for the nonadiabatic behavior of the initial pulse.

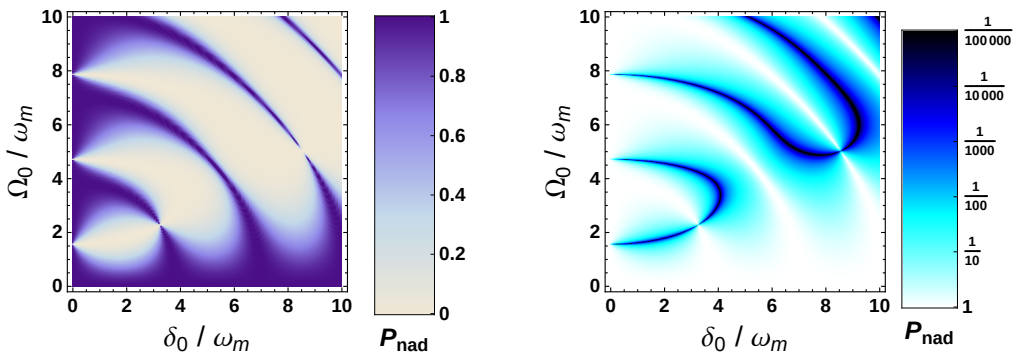

(a) linear (b) logarithmic

Figure 3.7: These new structures appear within a few cycles. Changes are already visible after one complete sequence (two pulses) and the structure manifests within 10 cycles. The pictures shown here are the result of integrating over 25 cycles. This calculation neglected spontaneous emission.

Expressing single up and down sweeps in terms of rotation matrices, and combining them to a rotation matrix for a complete cycle yields the expected results. The combined rotation matrix for up-up has the same rotation axes as the matrix for a single up-pulse; the combined rotation matrix for up-down, on the other hand, can have its rotation axis (depending on Ω_0 and δ_0) close to the south pole. Everything mentioned is also valid for the opposite directions: down-down, and down-up, whose behavior is equivalent. The resulting force not only depends on P_{nad}, but it is individually dependent on the parameters Ω_0 and δ_0. This results in a new structure of the force map, which was already seen in Fig. 3.5 a). Theses features can be seen more clearly in Fig. 3.7, where

spontaneous emission was neglected.

Spontaneous emission has several effects. In regions where P_{nad} is small and the rotations would potentially yield a unstable up-up force over a long integration time, the initial coherence of the force is restored early enough (due to our pulse scheme with syncopation time) such that there is no difference between up-down and up-up sequences. Less ideal situations, like simply a point with bigger P_{nad} or a Doppler-detuned system, are more unstable and results in significantly lower or practically zero forces. Additionally spontaneous emission suppresses small resonance-like oscillations in force profiles or maps.

These tendencies have been confirmed in the Monte-Carlo distributions. A negative Rabi-frequency can also be considered to change the sweep direction. Whether or how this is experimentally accessible is questionable. Doing up-up sweeps in combination with Rabi-frequency being positive-negative yields an exact reversal of the initial sweep, resulting in the restoration of the ground state. Up-down sequences in combination with Rabi positive-negative yields alternate structures to only up-down in the force map.

An important question is whether the stability of up-down persists in experiment where spontaneous emission cannot be neglected, the pulse is not sinusoidal, the Rabi-frequency varies by about 10% over the whole interaction time, and we do not know the optical phase. Numerically we tried to model some of the effects individually and it seemed that although up-down sequences are affected, they are much more stable towards these processes. Of course there are a lot of other effects we did not account for, *i. e.* our two-level system is not perfect, and there might be significant contribution through

processes involving the 2^3P_1 level, especially at large sweep amplitudes and/or Doppler-detunings.

3.3.1 Non-constant peak Rabi frequency

In the experiment it is impossible to get a perfectly constant Rabi frequency over the whole interaction region, since we are using an Gaussian elliptical beam. The edges of the Gaussian profile are cut off by a vertical slit. We approximate the Rabi frequency in the remaining part to be parabolic

$$\Omega_0(z) = \Omega_0(1 - az^2) \tag{3.3}$$

where $z(t) = z_0(t/T_{int} - 1/2)$ is linear over the total interaction time T_{int} and the paramter a can be tuned such that there is a certain percentage at the edges. Mostly 90% was used. The results show a greater stability of up-down in contrast to up-up.

3.3.2 Random phases

The assumption that we can rotate the Bloch sphere in such a way, that the Rabi-frequency is completely real (and positive), can clearly not be hold in the experimental case, where the optical phase is somewhat uncontrollable. For that reason the most extreme case of completely random phases for individual pulses was investigated. The force was mapped for different peak Rabi-frequencies, detuning amplitudes and Doppler detunings.

The results, a sample is shown in Fig. 3.8, exhibited noise due to the randomness and the finite integration time. Several main features like the

superior stability of up-down in comparison to up-up and the asymmetry of the up-up force-profiles are still present. In the experimental situation, the phases might be correlated and that could lead to new characteristics. Random phases also make up-up more stable since the successive pulse is no longer the completely identical to the previous.

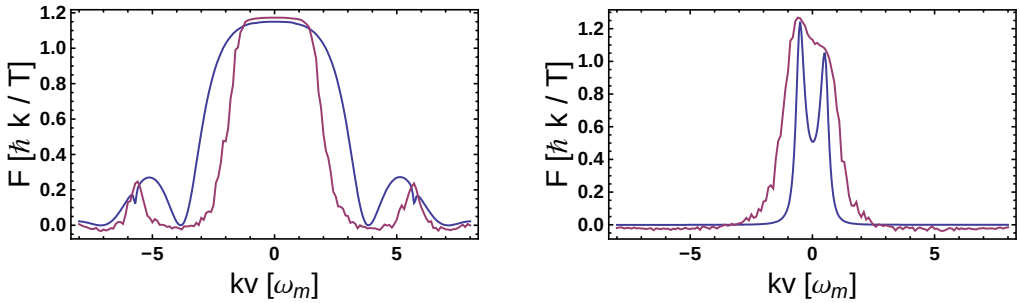

(a) Up-down (b) Up-up

Figure 3.8: The blue line shows the result for zero optical phase. In case of the purple line the phase of each pulses was set randomly. The simulation included spontaneous emission. The parameters were $\Omega_0 = 3.4\,\omega_m$ and $\delta_0 = 4.2\,\omega_m$.

Chapter 4

Vacuum System

Metastable Helium is produced by a reverse flow source [34], and travels down the beam line in a stainless steel vacuum system. The beam gets shaped and deflected in the interaction region, where the ARP light is brought into the vacuum. Further down the system, the deflection can be detected by a combination of multichannel plate (MCP) and phosphor screen (PS).

4.1 Beamline

Our lab has two metastable Helium beam lines: one is used for experiments on Rydberg atoms, while the other one is shared between our experiment and research on neutral atom lithography. The installation and stabilization of these was done during previous work [35].

The main beam line consists of a vacuum system assembled mostly out of 4" diameter stainless steel parts. We are using Conflat flanges which are sealed by copper gaskets. Our pressure is limited by the fact there a few O-ring

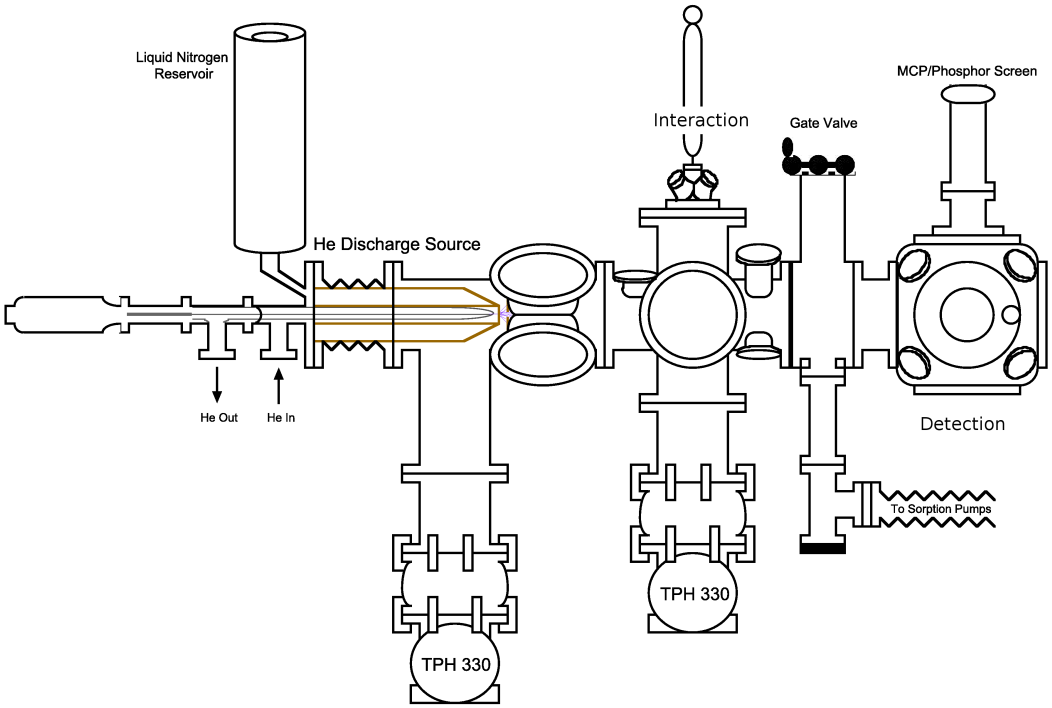

Figure 4.1: The first sixfold cross is used for the collimation of the lithography experiment and can be ignored for our setup. The interaction takes place in the second sixfold. The metastables are detected in the cube.

sealed flanges and that parts of the system are brought up to air regularly, for lithography purposes or maintenance. The system is directly pumped by two Pfeiffer Turbo pumps (TPH 330) which are backed by mechanical roughing pumps. Backing pressure of source and beam line is constantly measured by Convectron gauges. The absolute pressure can be measured by ion gauges which are controlled by Veeco Instruments Model RG830 gauge controller. Typical rest pressure is a few 10^{-7} Torr. The beam line can be separated into source, interaction and detection region.

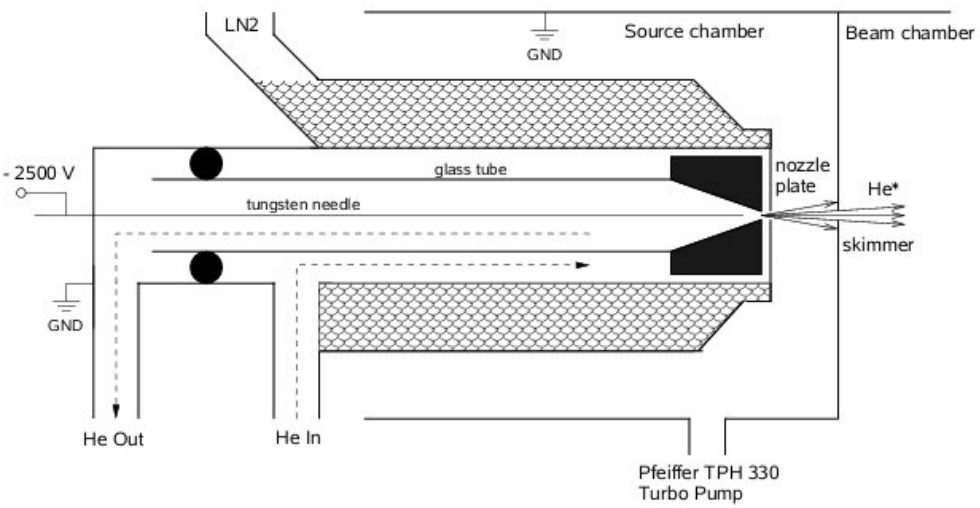

Figure 4.2: Schematics of the reverse flow metastable Helium source. Taken out of [12].

4.1.1 Metastable Helium source

Since the optical transition $1^1S_0 \rightarrow 2^3S_1$ is doubly forbidden and the energy difference is vast, metastable helium has to be produced by other means. This is done most efficiently by the use of a electric discharge. A reverse flow source, based on a DC discharge, has been designed by Kawanka et al. [34], which provides an intense beam of metastables. A modified version was built in Utrecht and is operated in our lab since 1999. A diagram of the source is shown in Fig. 4.2.

A 1 cm glass tube is mounted in the center of a 3 cm stainless steel jacket, which is cooled by liquid N_2. Helium flows between tube and jacket to the front, where the glass tube is narrowed. Teflon spacers keep the glass tube centered and force the helium against the outer wall of the jacket for further cooling. A Welch pump then pumps most of the helium back through an

opening in the front of the glass tube. Inside the glass tube is a tungsten rod that is kept centered by spacers. Sufficient flow is guaranteed by holes in the spacers. The rod is sharpened and its potential can be controlled by a DC power supply. A DC discharge is going from the tip of the needle to the nozzle plate. The electrons hit the Helium and generate a plasma. Amongst other things metastable Helium is generate. Inside the plasma the metastables decay quickly due to collisions. The only metastables that are not decaying are at a outside the plasma in its afterglow, outside the nozzle of the metal jacket, which is directly in front of tip. These are also more likely to proceed through the source chamber and into the beamline [36].

The source chamber basically consists of a T. The metastable beam enters the system on one side and travels through it. A skimmer plate on the opposite side blocks large parts of the beam, thereby limiting the angular velocity spread. At the lower end of the T the first Turbo pump is attached, which is backed by a mechanical pump. This pumps the excess atoms out of the system and also leads to differential pumping between the inner source and the source chamber. The T has an additional small window on top of the point, where the beam enters the source chamber, which enables us to monitor whether the source is lit.

Observing the operation of the source is possible because the discharge is also creating light, ions and electrons. Any charged particle can be deflected by either using permanent magnets, which can be attached to the outside of the vacuum system, or the use of deflection plates behind the skimmer plate, which are set under voltage. The light can serve as a reference in time of flight measurements using a chopper that is otherwise removed. This has been

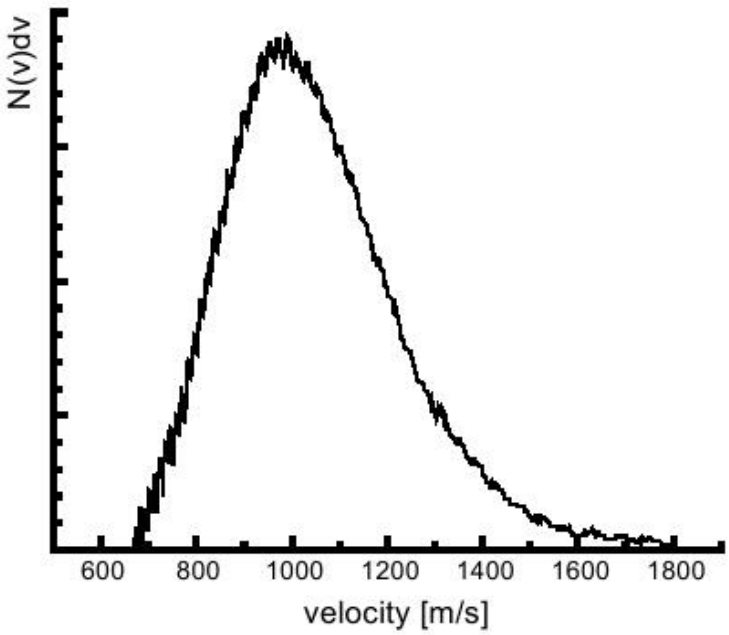

Figure 4.3: Velocity distribution of our metastable Helium beam. Figure taken out of [15].

done to measure the longitudinal velocity distribution of the metastables [35]. The results were reproducible and the distribution is shown in Fig.4.3. The distribution's maximum is at 1000 m/s and it has a FWHM of 400 m/s.

The efficient production of a bright metastable Helium beam is dependent on the specific setup of the source. The position of the tungsten needle, its voltage and the flow of Helium are parameters which have to be adjusted accordingly. Optimization of all parameters led to a usual metastable Helium beam of about 10^{14} atoms/(s sr) [15].

4.2 Interaction

The interaction between ARP light and atoms takes place in the second sixfold cross. The flanges in the horizontal plane, perpendicular to the beam, have windows which are AR coated for 1083 nm light. A vertical slit of width 250 μm cuts out a narrow part of the atomic beam with very low transverse velocity spread. This beam travels through Helmholtz-coils. The ARP light is brought onto the atoms along theiropen axes. The slit and the coils are mounted on a feed through on the top flange of the sixfold cross which enables us to lower them and see the detector when fully lit. The electrical connections for the coils are also on the top flange. Attached on the bottom of the sixfold cross is the second Turbo pump, which is backed by another mechanical pump. This provides the vacuum for the whole beam chamber.

The coils were designed and build in for previous work on ARP [12], where all the specifics can be found. A large enough $\vec{B}$-field ($\approx$ 7 Gauss splits the degeneracy of the magnetic fine-structure and provides an axis. This makes it possible to optically pump the atoms.

4.3 Detection

The detector is placed inside a cube with two view-ports. The cube can be separated from the rest of the system, giving us easy access for maintenance. This is done by a gate valve between the interaction region and the cube. The cube can be pumped individually by sorption pumps. The detector is mounted on a post which is attached on the top flange on another T on top of the cube.

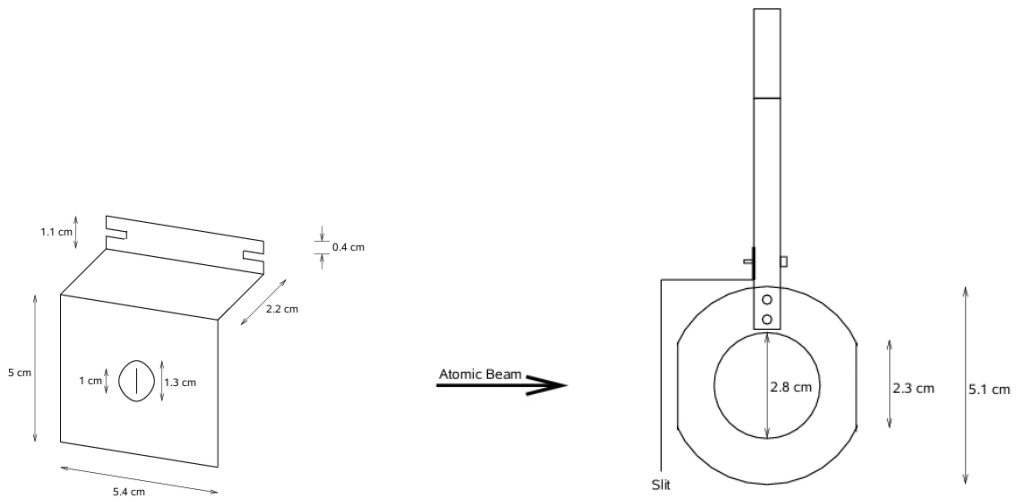

(a) Front view (b) Side view

Figure 4.4: a) The atoms pass the slit and go through the center of the coils perpendicular to their major axis. b) The light travels perpendicular to the plane and is brought on to the atoms in the center of the coils. Both figures were taken out of [12].

This T is either used to mount our detector or can contain a cold trap for the lithography experiment. The distance between the center of the coils and the front of the detector is 32 cm.

The detector consist of a micro channel plate(MCP) and a phosphor screen (PS). These are mounted between square stainless steel plates from Kimball Physics Inc. The plates are aligned by non-conducting aluminium oxide rods. Plastic spacers are used to separate the plates if necessary. Electrical connections are spot-welded onto the two plates holding the MCP and the front plate of the PS, and go to an electrical feed through. The front of the MCP is kept at negative voltages of approximately 700 V, the back is grounded and the front plate of the PS is at positive voltage of about 1200 V. The rods

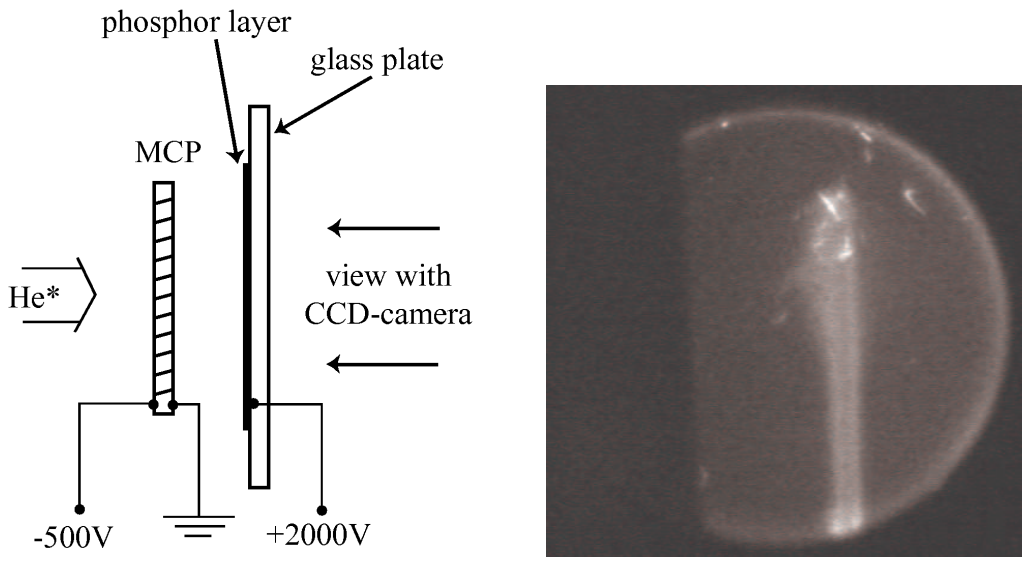

(a) Detector schematics

(b) Fully illuminated detector

Figure 4.5: a) Neutral metastables hit the MCP and eject electrons, which causes a cascade that can be made visible by fluorescence of a PS. Images are taken by a CCD camera. b) This is the background of the fully illuminated detector. It is showing burn-marks and scratches on the MCP of a detector. The detector schematics were taken out of [15].

are held by an aluminum piece that is connected to the post. A mirror is mounted at an 45° angle behind the phosphor screen that reflects the image of the phosphor screen through the view port out of the vacuum system and onto a CCD camera, which allows us to take pictures. The setup is shown in Fig. 4.5 a).

The MCP's were ordered from Burle Electro-Optics. Their active diameter is 0.96" and they consist of channels almost perpendicular to the surface. The channels are ordered in a hexagonal structure. When atoms with $E \approx 20\,\mathrm{eV}$ hit the MCP, they eject electrons out of the semi-conducting walls of the channels, which are accelerated by a maximum voltage of 1000 kV across the channel towards the next wall, where secondary electrons are ejected, etc. The gain depends on the voltage across the MCP. This avalanche leaves the MCP and is accelerated towards the phosphor screen.

Two different kinds of phosphor screens were used. The phosphor screens from Lexel Imaging Systems consist of a glass plate coated with layers of aluminum, indium tin oxide (ITO) and P43 phosphor. The aluminum diffuses charge, the ITO assure a good adhesive and conductive to the phosphor. When an electron cascade hits the phosphor, it causes fluorescence in the green, which can be observed by the CCD camera. The second type of PS used, was purchased from a private individual. It also consists of a glass plate, which is coated with a thin layer of gold and P20 phosphor on top.

The limitations of this detector are that the combination of MCP, PS and CCD camera lead to a highly non-linear behavior of the pixel intensity as a function of the atomic flux, which makes quantitative measurements extremely difficult. The MCP and PS can only be operated in vacuum below 10^{-5} Torr

and require a completely dry storage space. They show signs of aging and are burned if the atomic flux or the electron cascade is too large (Fig. 4.5 b)). The main advantage of the detector is that it is real time and that taking pictures is only a matter of seconds.

Chapter 5

Generation of ARP Light

The generation of ARP-pulses is key to this experiment. A distributed Bragg reflector (DBR) diode laser provides the 1083 nm light required for the $2^3S_1 \rightarrow 2^3P_2$ transition of metastable helium. This laser is locked by optical feedback, using a saturated absorption spectroscopy (SAS) signal. Phase modulators allow us to sweep and/or detune the frequency. Amplitude modulators give control over the amplitude of the light. Both modulator types are based on the electro-optic effect of lithium niobate ($LiNbO_3$). The spectrum of the modulated light is monitored with Fabry-Perot (FP) interferometers. Time-dependent intensities are resolved with fast photodiodes. Fiber amplifiers provide the required power.

5.1 Laser

In the experiment a Spectra Diode Labs SDL-6702-H1 DBR(distributed Bragg reflector) laser is used. High performance power of about 20 mW, tune-ability

via control of current and temperature and low cost are the diode's major advantages. The active region of the diode contains a grating which provides further frequency stability.

The diode laser is in an 8-pin TO-3 casing, in which a thermistor and thermoelectric cooler are included. The current is controlled by a Newport 505 current controller, which also allows us to modulate with low voltage signals at frequencies up to 500 kHz. The temperature of the diode is controlled by an Newport 325 temperature controller which keeps the (temperature dependent) resistance of the diode stable.

We were usually running the laser at a resistance $R = 9.79\,\mathrm{M\Omega}$ in the thermistor monitor and a current of $I \approx 137\,\mathrm{mA}$. The current varies on day to day basis, since our laboratory is connected to the buildings heating or air conditioning. This system's feedback is binary, which results in a 20 min temperature cycle. The humidity is not controllable.

The light out of the diode hits a 70:30 polarization independent beam-splitter. The 70% beam goes through a Faraday isolator and is coupled into a fiber which sends it to the modulation stages. The other 30% gets retro-reflected off a mirror on a PZT(piezo electric transducer). This extended cavity of adjustable length provides direct optical feedback, sending 9% of the light coming out of the diode back into the diode. The remaining 21% is sent through an optical fiber to a Helium glass cell. This setup is shown 5.1.

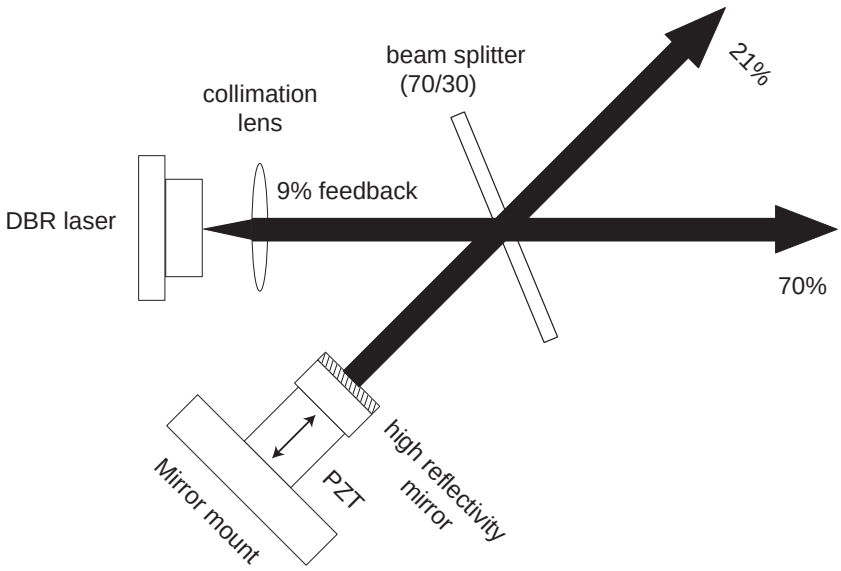

Figure 5.1: Extended cavity setup of our laser which provides stable frequency locking by electronic feedback. Figure out of [5].

5.1.1 Laser-Locking by SAS

To lock the frequency of the diode to the atomic transition we use electronic feedback. We have a He-cell in which an RF discharge provides metastables. A glass plate splits the original beam into 3 parts. Two go parallel to each other through the helium cell; these are called probe beams. The third, the pump beam, is steered around the cell and goes through the cell in the opposite direction, almost perfectly overlapping with one of the probe beams in the center of the beam and completely avoiding the other. The probe beams are weak and the pump beam is strong. When the light passes through the cell resonant atoms will absorb light. Moving atoms see Doppler-detuned light. The detuning they see is opposite if the light comes from the opposite direction. Therefore only atoms at rest can be resonant to pump and probe

beam (of the same frequency) at the same time. In this case the absorption of the overlapped probe beam is going to be suppressed, since the pump beam already saturates most of the atoms. We detect the intensity of the two probe beams with individual photo-diodes. We subtract the NOT-overlapped beam with the overlapped beam signal electronically, amplify this signal and send it to the locking electronics. This yields a Doppler-free signal. The schematics of the He-cell spectroscopy setup are shown in Fig. 5.2.

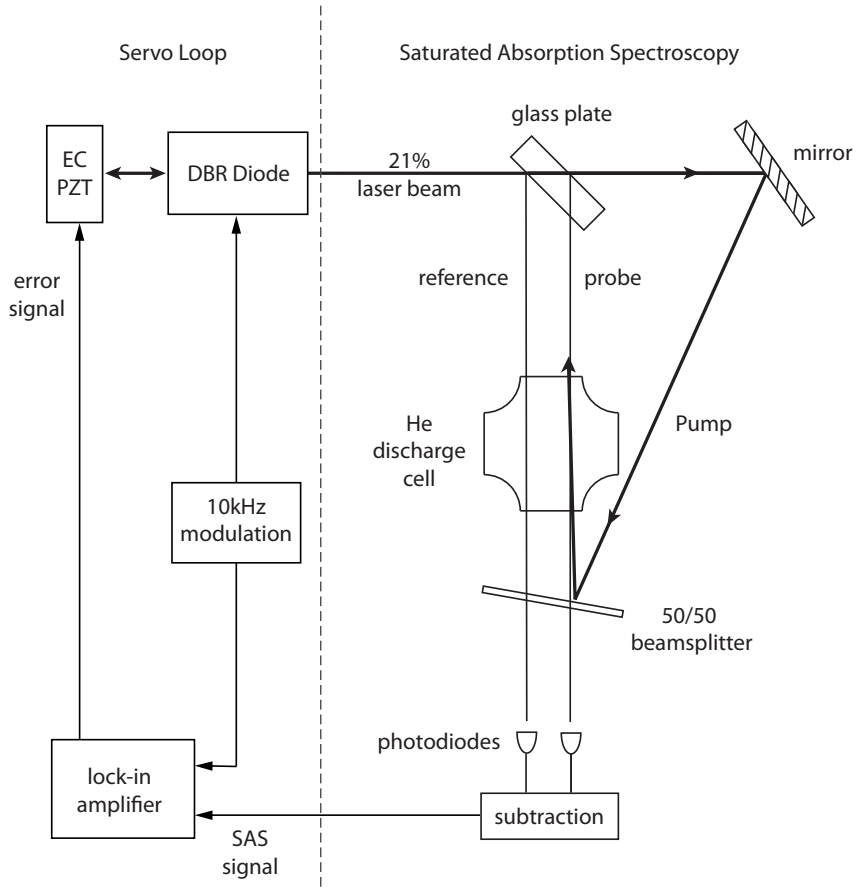

Figure 5.2: This setup enables us to lock the frequency of the laser to the desired transition for several hours. The linewidth is far below the Doppler width. Figure taken out of [5].

This so called SAS (saturation absorption spectroscopy) signal [37] is cleaned up by two successive, home-built, low pass filters. This signal is split and monitored on an oscilloscope. The other part is sent to a lock-in amplifier which provides an error signal. A proportional integrating differential controller (PID) is used to generate the feedback signal that is sent back to the Newport current controller.

Finally the laser frequency ω_l is locked to the atomic transition frequency $\omega_a = \omega_l$, and the line-width of our locked light is assumed to be 1.6 MHz, limited by the signal to noise ratio of our error signal. Under good condition, this setup is able to keep the frequency locked for several hours. This scheme was first set up by [38].

5.2 Electro optic effect

The creation of ARP pulses in this experiment is done by electro-optic modulators. Phase-modulators allow us to sweep and/or detune the frequency. Amplitude modulators shape the required pulses. We are using near infrared (NIR), fiber-coupled, integrated-optics modulators from Photline, which are based on lithium niobate ($LiNbO_3$). Proton exchange is used to create the waveguide between the electrodes. This is done by replacing Li^+-ions with protons when the crystal is exposed to an acid. The Au-Cr electrodes are separated from the crystal by a dielectric buffer. The integrated optics are sealed in a metal casing, which has SMA connectors for the RF signal. The whole modulators are placed in plastic boxes to shield/isolate them from the lab environment.

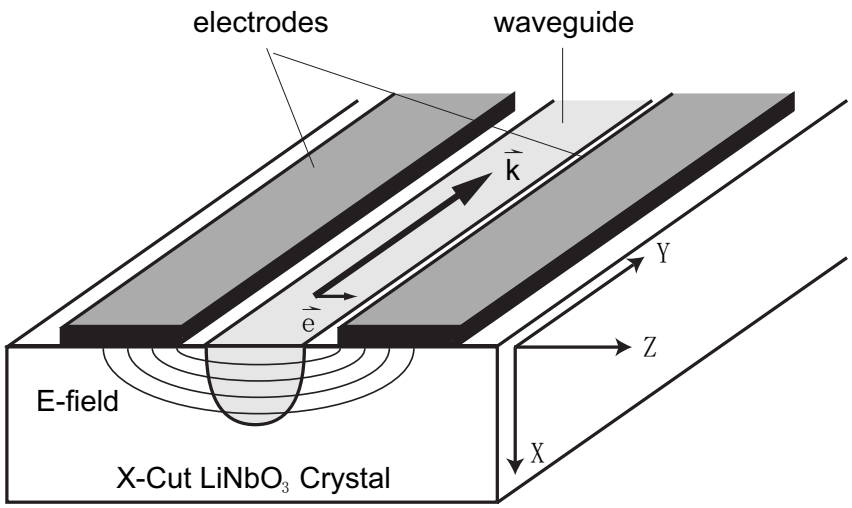

Figure 5.3: The polarized light travels along the Y-axis, the E-field of the RF signal and light field are both in the z-directions. The input fiber is polarization maintaining to assure the polarization of the input light. Figure taken out of [5].

The modulators make use of the linear electro-optic effect which changes the polarization-dependent index of refraction n proportional to the applied voltage V_{rf}. Varying the voltage results in a different phase φ (for light parallel the ordinary and extraordinary axis of the crystal). The interaction of this anisotropic crystal and arbitrarily polarized light is complex and can be generally described by a third rank tensor [39]. All our modulators are x-cut and use fiber, which is polarization maintaining (Panda style) on the input side. This results in extraordinary, linearly polarized light, whose electric field is parallel to the applied RF-field and one of the principal axes of the crystal, as illustrated in Fig. 5.3. Under these conditions only one element of the tensor is sufficient to describe the phase-modulation $\varphi(V_{rf})$. This configuration makes use of the strongest component $r_{33} = 32\,\mathrm{pm/V}$ of the tensor describing $LiNbO_3$, in order to achieve the maximal effect.

The overall time-dependent phase can be written as

$$\varphi(t) = \kappa M(\omega_{rf}) V_{rf}(t) \tag{5.1}$$

where $M(\omega_{rf})$ is a dimensionless parameter that accounts for the frequency dependence, since there are RF losses and the phase between driving RF and the driven optical properties of the crystal are not constant. $\kappa = \frac{\pi}{\lambda G} n_e^3 r_{33} \eta L$ describes the properties of the modulator: G is the gap between and L length of the electrodes. It becomes apparent again, that the use of integrated optics, where the gap width G is rather small compared to those in free space electro optic modulators, is beneficial, since it is possible to achieve considerable phase-changes with comparably low RF signals. The parameter n_e is the

index of refraction for extraordinary light, r_{33} is the electro optic coefficient of $LiNbO_3$. The overlap between the electric fields of the light and RF signal is described by η. For a detailed discussion of this factor I referred to the PHOTLINE web-page[1].

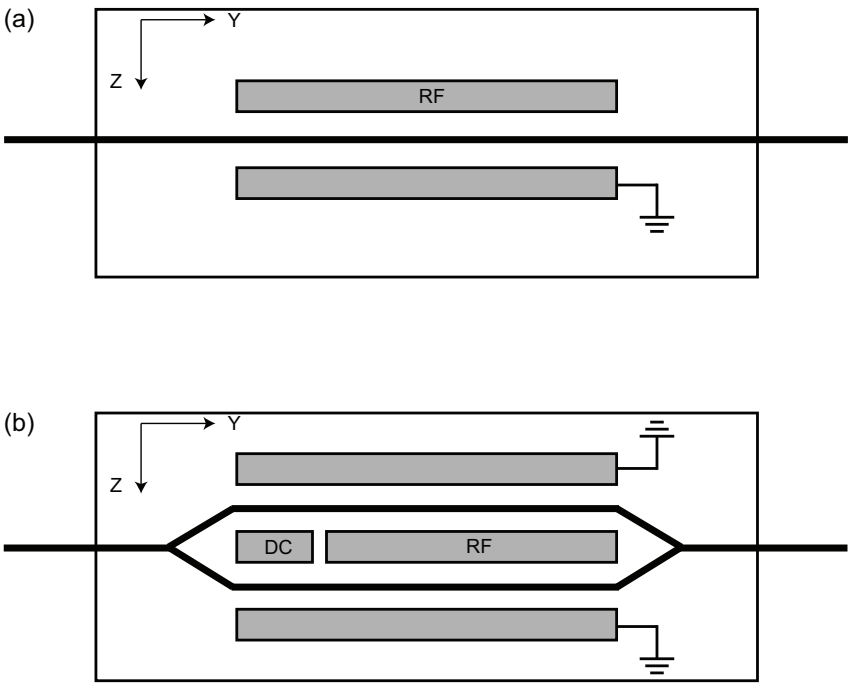

Figure 5.4: Basic schematics of the electro optic modulators. a) Shows the PM consiting of only one waveguide. Applying a voltage on the electrodes changes the index of refraction of the crystal. If this is time dependent the optical phase of the light in the modulator is shifted. The AM, which is basically a MZ interferometer, is shown in b). Figures taken out of [5].

5.2.1 Phase Modulation

The phase modulator NIR-MPX-LN03 from PHOTLINE consists of one single waveguide enclosed by two electrodes, one grounded, the other one connected

[1]http://www.photline.com

to the RF signal as shown in Fig. 5.4. Applying a RF signal results in a phase $\varphi(t)$, which is equivalent to frequency modulation, since the time derivative of the phase yields a time-dependent detuning $\delta(t)$ from the laser frequency ω_a

$$\omega(t) = \omega_a + \frac{\partial \phi(t)}{\partial t} = \omega_a + \delta(t). \tag{5.2}$$

If the phase is given according to Eq. (5.1) and a sinusoidal RF signal with amplitude V_0 and frequency ω_m is applied, the detuning becomes

$$\delta(t) = \omega_m \beta(V_0) \cos(\omega_m t) = \delta_0(V_0) \cos(\omega_m t) \tag{5.3}$$

with

$$\beta = \kappa M(\omega_m) V_0 \tag{5.4}$$

This yields continuous modulation of the phase by the sinusoidal RF signal, as assumed in Sec. 2.2. Note the dependence on the frequency, which requires us to determine $\beta(V_0)$ experimentally. In order to do that, it is useful to look at the Fourier components of our sinusoidally modulated light, which are given by the Jacobi-Anger [40] expansion

$$E(t) = E_0 \cos\left[\omega_a t - \beta \sin(\omega_m t)\right] = E_0 \sum_{k=-\infty}^{\infty} J_k(\beta) \cos\left[(\omega_a + k\omega_m)t\right]. \tag{5.5}$$

This results in a spectrum of sidebands which are equally spaced by ω_m and whose frequency components' amplitudes are symmetric around the center frequency ω_a, since $J_{-k} = (-1)^k J_k$. Another property of Bessel functions is

the recurrence relation

$$J_{n+1}(\beta) + J_{n-1}(\beta) = \frac{2n}{\beta} J_n(\beta) \tag{5.6}$$

which allows one the calculation of β out of three neighboring peaks. Fabry-Perot measurements need to be done over the accessible range of voltages to determine $\beta(V_0)$ at our operating frequency ω_m. The calibration of the first phase-modulator can be found in [5]. A second one was purchased this year and compared to the first one. Its calibration curve is shown in Fig. 5.5. They show slight differences, which was neglected. Depending on the RF-setup, the differences can be corrected by splitting their RF-signal into parts of unequal intensities.

A parameter commonly used to describe the performance of a phase-modulator is

$$V_\pi = \frac{\lambda G}{n_e^3 r_{ee} \eta L M(\omega_m)} \tag{5.7}$$

which is the voltage at which $\beta = \pi$. Extrapolating from Fig. 5.5 we obtain the voltage of the signal generator $V_{\pi,SG} = 23\,\mathrm{mV}$ at which $\beta = \pi$. This leads to the true value of $V_\pi = 3.7\,\mathrm{V}$ after amplification.

5.2.2 Amplitude Modulation

Amplitude modulation is achieved by electro-optic modulators (PHOTLINE NIR-MP-LN03), that are Mach-Zehnder (MZ) type [37], integrated-optics interferometers. The basic configuration of a amplitude-modulator is shown in Fig. 5.4. The two paths pick up opposite phase shifts $\pm\beta$, and their interfer-

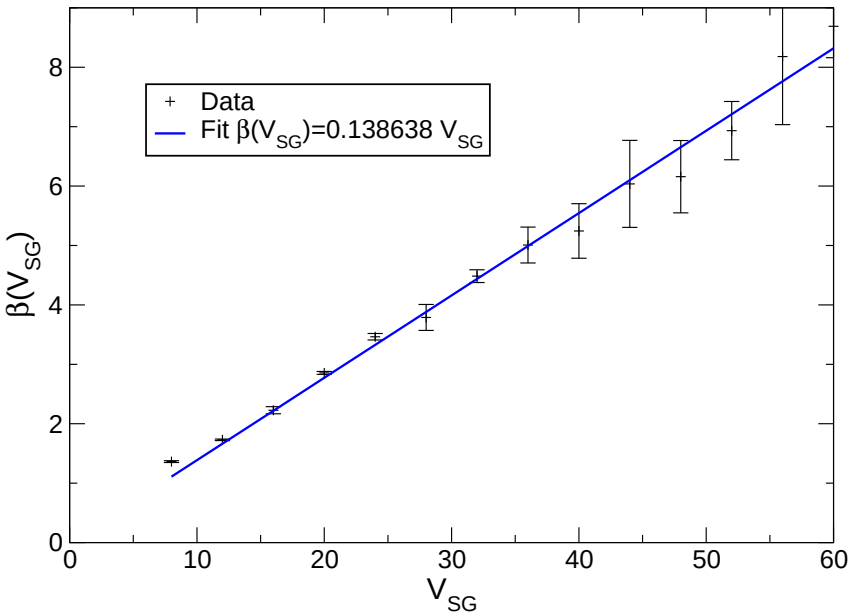

Figure 5.5: The intensity of each side peak in a Fabry Perot (FP) interferometers spectrum is extracted for various RF amplitudes. These are given by the amplitude of the signal generator V_{SG}. According to Eq. (5.4) we expect β to be approximately linear in V_{SG}. Equation (5.6) enables us to calculate the parameter β out of three successive peaks of the Fabry Perot spectrum. The plotted values are an average over every accessible combination of three peaks for the corresponding RF amplitude.

ence can be calculated as,

$$E = \frac{E_0}{2}\Big[\cos\big(\omega_l t + \beta(t)\big) + \cos\big(\omega_l t - \beta(t)\big)\Big] = E_0 \cos\big(\omega_l t\big)\cos\big(\beta(t)\big) \tag{5.8}$$

where $\beta(t)$ is proportional to the applied voltage $V(t)$. The output power becomes

$$P(\beta) = \frac{P_0}{2}\big[1 + \cos(2\beta)\big], \tag{5.9}$$

where P_0 is the maximal power. This function is shown in Fig. 5.6 a) and yields the desired envelope, Eq. (2.3a), for a triangle pulse. The AM has an

extra electrode that facilitates the possibility to set an operating point, by applying a DC voltage. The result is an offset phase $\beta(t) = \beta_{dc} + \beta_{rf}(t)$. For the purpose of pulse generation an extremal operating point (MIN or MAX) is preferred, since pulses of maximum amplitude and a bias field as low as possible are required. Due to superior stability a minimum is used. Note that only a phase shift of $\pi/2$ per arm and therefore a voltage $V_\pi/2$ is required to switch from minimum to maximum transmission.

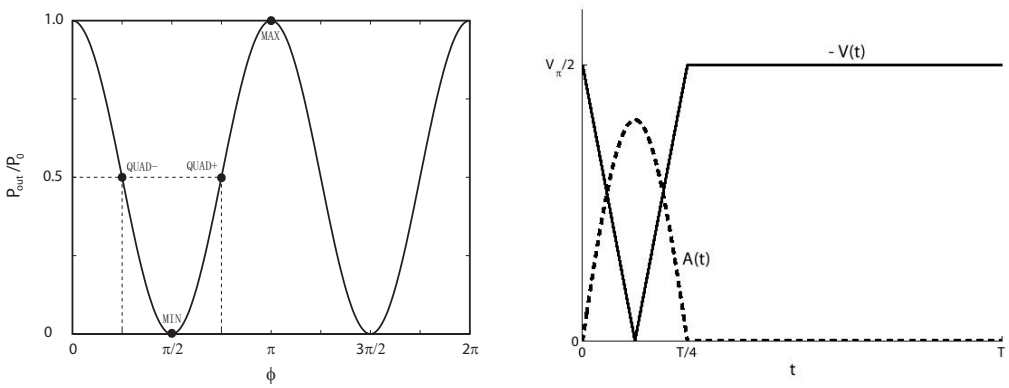

(a) Transmitted power dependent on phase β

(b) Ideal in- and output of the AM for ARP pulses

Figure 5.6: The sinusoidal transfer function of a Mach-Zehnder type interferometer is shown in a). A DC can be used as an offset in phase. Our ideal time dependent in- and output of the MZ interferometer is shown in b). Figures taken out of [5].

Upon applying a (almost) perfect triangle wave and using a 25% duty cycle, the amplitude of the electric field is given by

$$E(t) = E_0 \exp(\mathrm{i}\omega_a t) \begin{cases} \sin(\omega_m t) & \text{, for } 0 \leq t \leq T/4 \\ 0 & \text{, for } T/4 < t \leq T \end{cases} \tag{5.10}$$

The electric field of our AM light can then be described by the usual Fourier

series, yielding the intensity of the nth (side) peak of our spectrum

$$I_{FP,n} = \left(\frac{4}{4-n^2}\right)^2 \cos^2\left(\frac{n\pi}{4}\right). \tag{5.11}$$

In opposition to the the purely phase modulated light, the amplitude modulated light has sidebands at all multiples of the repetition frequency ω_c. Our pulses are not perfectly sinusoidal. They show tails and a small damped oscillation after the trailing edge. This can be seen in Fig. 5.8 a). In contrast to expectation the FP signal of these pulses looks surprisingly good and symmetric (Fig. 5.8 c)).

5.3 Light Analysis

After modulating, we have to assure the quality of our light. The amplitude modulation and the delay of the optical pulses in the interaction is monitored by fiber coupled fast photodiodes from Thorlabs. The spectrum is analyzed by Fabry Perot (FP) interferometers [9, 37]. These were home built and are described in more detail in [5]. Their most important aspect is the free spectral range of 3 GHz, which allows us to resolve individual side peaks as well as cover the required range of several modulation frequencies.

To explain certain properties of the expected spectrum, I will first calculate their Fourier expansion. Generally we assume a electric field, that is both phase- and amplitude-modulated

$$E(t) = A(t)\cos\big[\omega_l t + \varphi(t)\big], \tag{5.12}$$

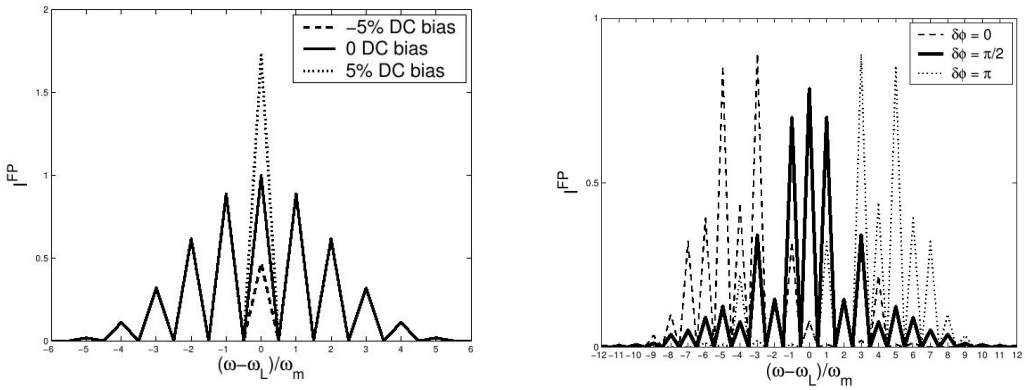

(a) Effects of a bias light field

(b) Phase dependence between PM and AM

Figure 5.7: The figures show calculated FP spectra. a) A bias light field largely affects the carrier frequency. b) Adjusting the phase shifts the center of spectrum. They are taken out of [5].

where $A(t)$ and $\varphi(t)$ are both periodic in $T_c = \frac{2\pi}{\omega_c}$, which allows us to write $E(t)$ as a Fourier series

$$E(t) = \sum_{n=-\infty}^{\infty} \left[c_n \mathrm{e}^{\mathrm{i}(\omega_l + n\omega_c)t} + c_n^* \mathrm{e}^{-\mathrm{i}(\omega_l + n\omega_c)t}\right]. \tag{5.13}$$

with the coefficients given by

$$c_n = \frac{1}{T} \int_0^T E(t) \exp\bigl(-\mathrm{i}(\omega_l + n\omega_c)t\bigr) \mathrm{d}t \tag{5.14}$$

The complex formulation is the simplest, because it requires only one coefficient for the calculation of the intensity of our (side) peak, which is what is measured by our Fabry Perot (FP) interferometers

$$I_{FP,n} = \left|2c_n\right|^2 \tag{5.15}$$

Two important aspects which are always monitored are shown in Fig. 5.7. Depending on how well the operating point of the AM is set, a bias light field might be present that makes periodic ARP processes impossible. The result of bias light fields on the spectrum is shown in part a). The phase between amplitude and detuning as shown in part b), can also be observed on the spectrum , since it shifts the center of the spectrum. A “good” ARP pulse is symmetric about the carrier frequency. Typical measurements of the fast-photo diode and FP spectra are shown in Fig. 5.8. All of them were recorded with a fast digital scope from LeCroy.

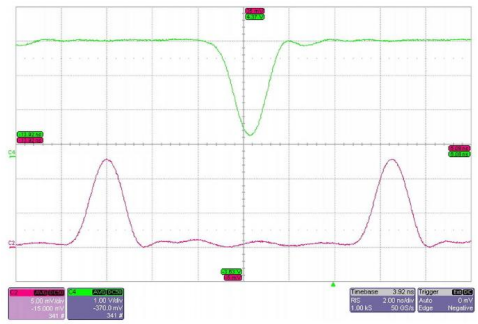

(a) Fast-photo diode signal

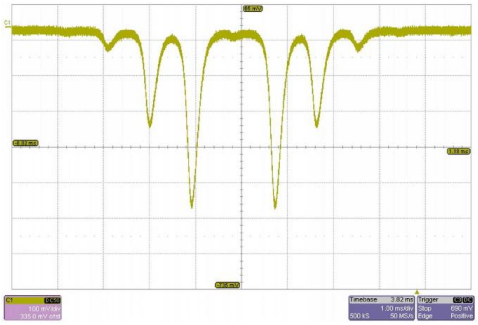

(b) FP signal of phase modulated light

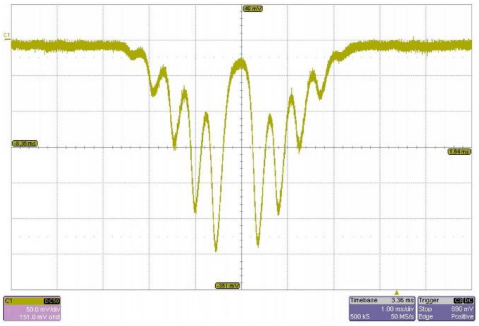

(c) FP signal of amplitude modulated light

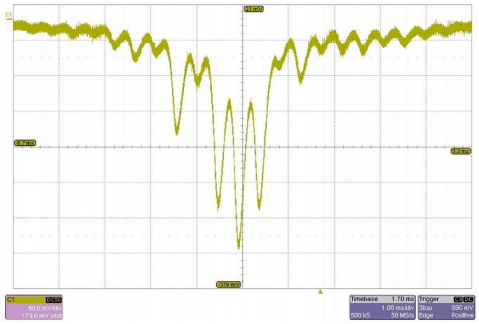

(d) FP signal of swept ARP pulses

Figure 5.8: a) and d) are constantly monitored. b) and c) are useful for debugging purposes. Figures were taken out of [5].

5.4 Light Setup

Light modulation and losses in other optical elements require us to have additional amplification on our setup. Both electro-optic modulator types have 3 dB insertion loss. Amplitude modulation results in additional losses of $\approx 87\%$. The maximal input of the phase (amplitude) modulator is 100 mW (500 mW). Of the 20 mW out of the diode, only about $5 - 6$ mW make it to the modulation region. These can be either amplified immediately or after the phase modulator by a 1 W fiber optical amplifier (Optocom Innovation), which can be safely turned up to $200 - 300$ mW. Amplitude modulation follows. We mostly use optical fibers to transport our beam. Theoretically all the modulation could be done in a system consisting only of fibers. The major losses occur at the fiber couplings or matings. Our fibers couplers are generally angle polished cut (FC/APC). Nethertheless, after all modulation stages, approximately $0.5 - 1.5$ mW of optical power remain. A general diagram of the setup is shown in Fig. 5.9.

Two Ytterbium based, 5 W fiber amplifiers from Keopsys (KPS-BTQ-YFA-NLS-1083-40-COL) are providing the intensities required for ARP. Their specifics are discussed in more detail in [5]. Ytterbium doped fiber is pumped by diodes, whose current can be controlled. There are three stages: a pre-amp, which cannot be controlled, and two diode pump lasers for the main amplification of which the second one is never used. The amplifiers show slight spectral inhomogeneities, which can only be corrected by adjusting phase and offset until our FP spectra are as symmetric as possible. Their output is shaped in telescopes, which were originally setup up for the lithography experiment.

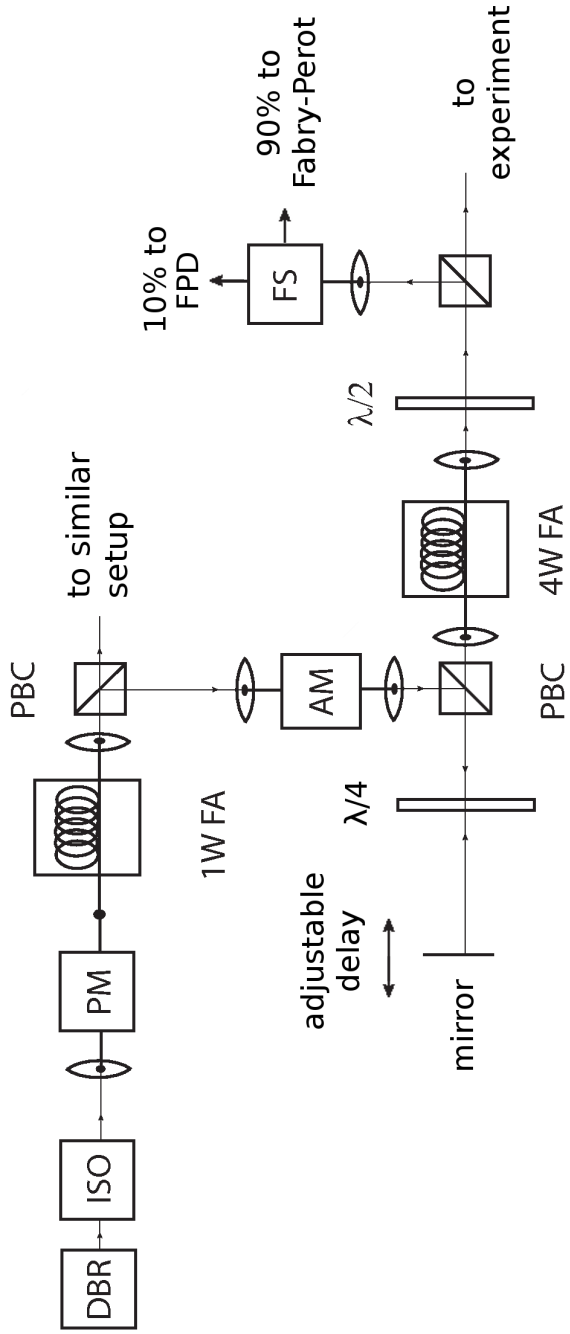

Figure 5.9: A possible setup for a two beam ARP run. The order PM and 1 W FA can be switched. An additional PM leads to completely individual modulation lines. This pictures was modified. Its original was taken out of [5].

Flip-mirrors pick off the beam and send it to our interaction region. Figure 5.10 shows a simplified scheme. Shaping the beam profile results in a Gaussian elliptical beam profile, with very low divergence (long Rayleigh range).

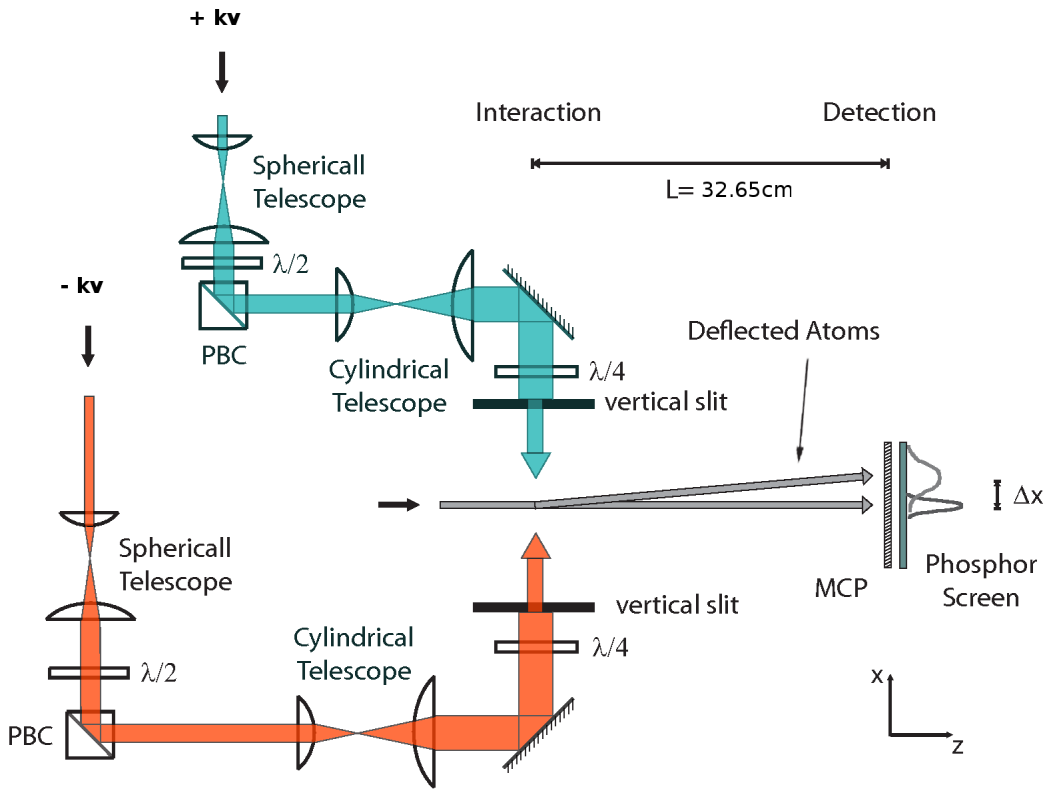

Figure 5.10: Coming from the 5 W FA, the beams are shaped by in spherical and cylindrical telescopes. They are overlapped in the interaction region, deflecting atoms, which is detected by our MCP/PS detector. This pictures was modified. Its original was taken out of [5].

Chapter 6

Measurement of the Force

After describing the details of our experimental setup, I now want to turn to the big picture: Which experimental values are taken during an ARP run and how can we extract certain properties of the ARP force from this data?

6.1 Deflection

Since the force is measured through deflection, it is useful to define a coordinate system: z is in the horizontal direction of the atomic beam. x is in the horizontal direction of light propagation in which the atoms are pushed. y is vertical in the lab frame.

Using the detector described in Sec. 4.3, we are able to measure the deflection Δx of the atomic beam. This deflection results from the transverse velocity change Δv_t due to the force during the the time t_{int} the atom is in the interaction region. Assuming that the interaction time is short compared to the flight time (since the interaction region $l_{int} = 4.0\,\mathrm{mm}$, is small compared

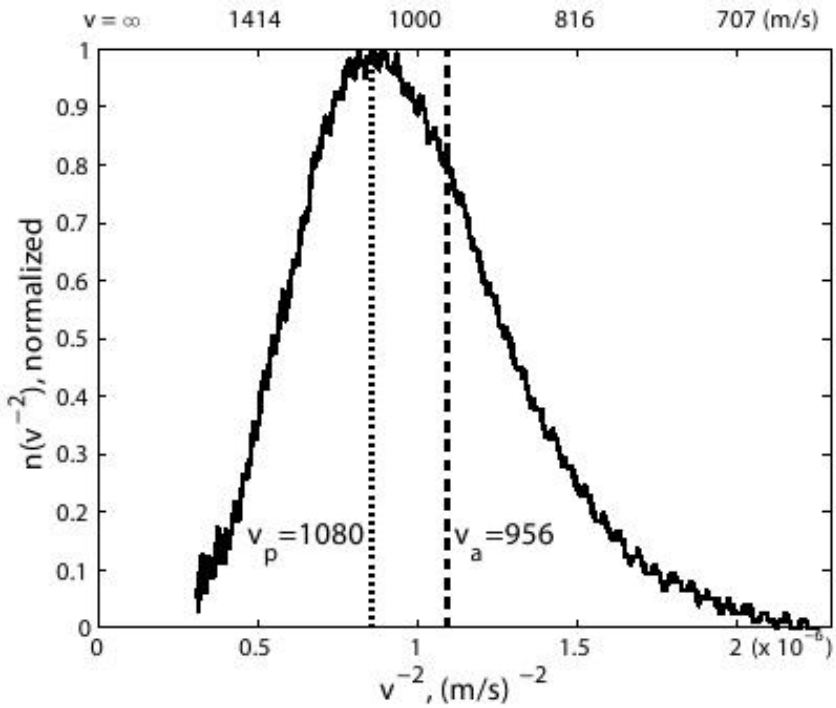

Figure 6.1: Distribution of the squared, inverse velocity. The maximum at $v_{max} = 1060\,\mathrm{m/s}$ and the average at $\bar{v} = 956\,\mathrm{m/s}$ are not the same as in the distribution shown in Fig. 4.3. Figure taken out of [12].

to its distance to the detector $l_{flight} = 32\,\mathrm{cm}$) the deflection becomes

$$\begin{aligned}\Delta x = v_t \cdot t_{flight} &= \frac{F_{ARP}}{m_{He}} \cdot t_{int} \cdot t_{flight} \\ &= \frac{F_{ARP}}{m_{He}} \frac{l_{int}}{v_l} \frac{l_{flight}}{v_l},\end{aligned} \tag{6.1}$$

where the force and the longitudinal velocity v_l are distributions. The velocity distribution mentioned in Sec. 4.1.1 leads to the distribution for v_l^{-2} shown in 6.1. This all leads to a smeared out deflection Δx.

The deflection pictures and backgrounds are taken. The pictures are subtracted, peak and mean deflection are extracted. To simplify, we assume that

the actual velocity change is small compared to the capture range of the force. We furthermore neglect the initial transverse velocity spread out of the slit for the atomic beam $v_{t,0}$. Since our detector is non-linear, it is useful to only look at maximum and/or average of the deflection and try to extract the maxima/mean of the force.

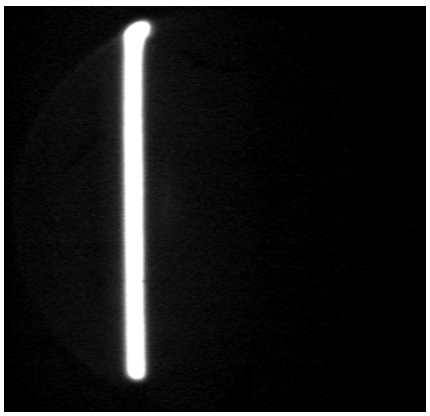

Figure 6.2: Undeflected atom-beam which is subtracted for analysis. Figure taken out of [12].

6.2 Parameters

We are measuring the time averaged power of our laser light $\bar{P}$ and need to relate this to our peak Rabi frequency Ω_0, since we have no detector capable of measuring such high powers, at the time scale of nanoseconds. The Rabi-frequency is related to the intensity by

$$\frac{I}{I_s} = 2\left(\frac{\Omega}{\gamma}\right)^2 \tag{6.2}$$

where $\gamma = 2\pi \times 1.6\,\mathrm{MHz}$, and saturation intensity $I_s = 0.167\,\mathrm{mW/cm^2}$, which was calculated for the specific transition.

A cylindrical telescope is used to set a Gaussian beam with waists of $w_y = 2.1\,\mathrm{mm}$ and $w_z = 7.0\,\mathrm{mm}$. The intensity is described by

$$I = I_0 \cdot \exp\Big(-\frac{2y^2}{w_y^2} - \frac{2z^2}{w_z^2}\Big) \tag{6.3}$$

The average power $\bar{P}$ can therefore calculated by integrating over the spatial dimensions x,y and and the time t

$$\begin{aligned}
\bar{P} &= \frac{1}{T}\int_0^T \mathrm{d}t \int_{-\infty}^{\infty} \mathrm{d}y \int_{-\infty}^{\infty} \mathrm{d}z\, I_0(t) \exp\Big(-\frac{2y^2}{w_y} - \frac{2z^2}{w_z}\Big) \\
&= \frac{\pi}{2} w_y w_z \cdot \frac{1}{T}\int_0^T \mathrm{d}t\, I_0(t) \\
&= \pi w_y w_z \cdot \frac{I_s}{\gamma^2} \cdot \frac{1}{T}\int_0^T \mathrm{d}t\, \Omega(t)^2
\end{aligned} \tag{6.4}$$

We are assuming a 25% duty cycle and take $\Omega(t) = \Omega_0 f(t)$ with $f(t) = \sin(\omega_m t)$ for the first 25% of our duty cycle and zero during the remaining 75%. Therefore the integral yields $\int_0^{T_c/4} \mathrm{d}t\, \sin^2(\omega_m t) = 1/8$. The final relation between average power and peak Rabi-frequency becomes

$$\bar{P} = \frac{\pi}{8} w_y w_z I_s \left(\frac{\Omega_0}{\gamma}\right)^2 . \tag{6.5}$$

During an ARP run, both 5 W fiber amplifiers are turned up and matched to the maximum optical power we want to use. A half-wave plate and a successive

polarizing beamsplitter cube (PBC), before each telescope, allow us the fast adjustment of the power.

Controlling the detuning amplitude δ_0 is easier. The function generator for the phase-modulators is digital and can be stepped up. The peak voltage V_0 is recorded and can be correlated to the detuning amplitude, by the calibration shown in Fig. 5.5.

6.3 Setup

All our RF-equipment that provides the necessary signals for the electro-optic modulators is triggered off the signal generator of the phase-modulator. The phase-modulators need a comparably high voltage, which is provided by an RF-amplifier. We have multiple RF-pulse generators (HP8082A), which permit the generation of the required pulse sequence. One of their controls adjusts the phase (between amplitude- and phase-modulation). The right phase between amplitude modulation and phase modulation can be set by symmetrizing the Fabry-Perot signals.

After shaping the required ARP pulses, we must now synchronize the pulse sequence in the interaction region. For this purpose a fast-photo diode was set up in front of the vacuum system, to relate the local pulse delay to the pulse delay in the interaction region. This delay was also related to the measurements of fiber coupled fast-photo-diodes, which are used to continuously monitor the pulse shape and the delay. The delay itself can be adjusted by a free space optical delay stage after one of the modulation beam lines.

Our usual repetition rate is $\omega_c = 2\pi \times 80\,\mathrm{MHz}$ and we are modulat-

ing/sweeping our frequency with $\omega_m = 2\pi \times 160\,\mathrm{MHz}$. According to Eq. (2.7) the maximum ARP force of this settings becomes $F_{ARP,max} = 16F_{rad,max}$.

6.3.1 Observation of ARP

The ARP experiment was inactive for a complete year. To start up again, the old scheme, with a retro-reflected beam, was set up again and the measurements were partially reproduced. A deflection image is shown in Fig. 6.3. Our maximum force corresponded to the previous experimental results of about $F_{ARP} \approx 6F_{rad}$. A complete mapping was omitted to proceed more quickly on to capture range measurements.

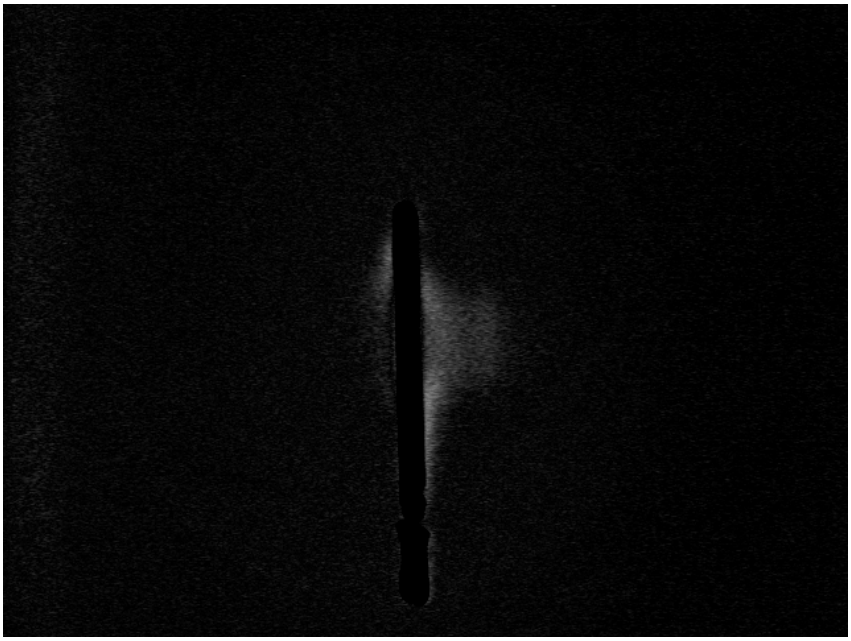

Figure 6.3: Deflection image taken with the CCD camera. The background was subtracted.

6.3.2 Capture range measurements

To measure the velocity dependence we transform our light into a frame, where atoms moving transverse to the atom beam at velocity v would be on resonance and atoms with no transverse velocity see Doppler-detuned light. This is done by detuning the two counter-propagating beams by the same amount $\delta_{kv} = \vec{k} \cdot \vec{v}$ and opposite signs $\pm\delta_{kv}$.

The first attempt on detuning was made using an acousto optic modulator(AOM). It is set at the Bragg-angle to maximize the power of the deflected beam. The deflected beam is being picked off and coupled into a fiber to the phase-modulator. The undeflected beam is retro-reflected into the AOM, which is now automatically set at the angle that maximizes the power of the oppositely detuned beam. To take care of back-reflections into the laser or the fiber-amplifier, the beam first goes through a polarizing beam-splitter cube (PBC), into the AOM and through a quarter wave plate at 45° angle. The polarization of retro-reflected beam is turned by 90° after passing the quarter wave plate for the second time, and will therefore be reflected and not transmitted by the PBC. This attempt failed because of power issues and the uncontrollable behavior of the 1 W fiber amplifier.

Another scheme makes use of our electro optic phase modulators. These can be used to detune a pulse if the slope of the applied voltage is constant for the duration of the pulse. A first approximation would be a sine wave of frequency $\omega_m/2$. Either a separate phase-modulator is used or the detuning signal is added to the sweeping signal and both can be done in one modulator. A RF-trombone matches the phase between both signals and assures that

sweeps occur during the linear part of the detuning signal. Numerical simulations show, that this approximation yields comparable forces and capture ranges. Problematic about this setup is, that the phase modulators maximum RF-input power limits our capability to detune and sweep by large amounts at the same time. One of our two phase modulators broke, probably due to reflections of a broken fiber end, which caused the connection between input fiber and crystal to explode.

6.3.3 Comparison of sweep directions

After the phase-modulator broke, we tried to do test whether the sweep direction is experimentally relevant or not. Both, up and down pulses, have the same Fabry-Perot signal, which is symmetric around the carrier frequency. The spectrum of up(down)-pulses shifts to higher(lower) frequencies for a small positive phase. Up and down pulses can therefore be distinguished by varying the phase on the RF- pulse generators while observing the behavior of the Fabry-Perot signal. After setting the correct sweep directions, the delay needs to be adjusted again.

Both beam lines were aligned, such that the beams would overlap in the interaction region. A small force was seen. Successive mapping for both up and down pulses was not possible due to temperature problems when the AC of the physics building broke.

Chapter 7

Conclusion

In this thesis the importance of the sweep direction in adiabatic rapid passage (ARP) sequences is discussed. Numerical studies by the integration of the optical Bloch equations were performed, where the atomic state is described by the Bloch vector. It was discovered that alternating the sweep direction of successive pulses results in a much more stable behavior of the Bloch vector, in comparison to only using one sweep direction. This is important for strong optical forces, since the atomic system needs to exchange its momentum coherently with the radiation fields.

The numerical studies were first done under the ideal assumption that spontaneous decay and other (experimental) perturbations can be neglected. The differences between using only one sweep direction and using alternating sweep directions is explained, by describing the time evolution during one pulse as a rotation of the Bloch sphere [30]. Using only one sweeping direction results in accumulating an error whereas the use of alternate sweeping directions can counteract imperfect passages. Gradually spontaneous decay and

other effects were included in the numerical simulations to test whether the prediction is still holding up under normal conditions. The differences between both schemes were still present. The introduction of randomness (spontaneous decay) stabilizes the time evolution and therefore the force if only one sweeping direction is used.

The experimental setup was extended to two modulation beamlines. The individual control of each beamlines' parameters enables one to compare one and alternating sweeping directions or do velocity dependence measurements. I hope that experimental data will become available. It will be interesting to see whether it is possible to observe the effects of the sweep direction in the laboratory.

Bibliography

[1] C.S. Adams and E. Riis. Laser cooling and trapping of neutral atoms. *Prog. Quantum Electron.*, 21:1, 1997.

[2] M. Partlow, X. Miao, J. Bochmann, M. Cashen, and H. Metcalf. Bichromatic slowing and collimation to make an intense helium beam. *Phys. Rev. Lett.*, 93:213004, 2004.

[3] M. R. Williams, F. Chi, M. T. Cashen, and H. Metcalf. Measurement of the bichromatic optical force on rb atoms. *Phys. Rev. A*, 60(3):R1763–R1766, Sep 1999. doi: 10.1103/PhysRevA.60.R1763.

[4] X. Miao, E. Wertz, M. G. Cohen, and H. Metcalf. Strong optical forces from adiabatic rapid passage. *Phys. Rev. A*, 75(1), jan 2007. ISSN 1050-2947. doi: {10.1103/PhysRevA.75.011402}.

[5] Xiyue Miao. *Optical Force on Atoms with Periodic Adiabatic Rapid Passage Sequences*. PhD thesis, State University of New York Stony Brook, August 2006.

[6] I. I. Rabi. Space quantization in a gyrating magnetic field. *Phys. Rev.*, 51, 1937.

[7] N. F. Ramsey. *Molecular Beams*. Clarendon Press, Oxford, 1956.

[8] M. O. Scully and M. S. Zubairy. *Quantum Optics*. Cambridge University Press, Cambridge, 1997.

[9] Peter W. Milonni and Joseph H. Eberly. *Lasers*. Wiley Interscience, 1998.

[10] L. Allen and Joseph H. Eberly. *Optical Resonance and two-level atoms*. Dover Publications, Inc., 1987.

[11] Richard P. Feynman, Frank L. Vernon, and Robert W. Hellwarth. Geometrical representation of the schrödinger equation for solving maser problems. *J. Appl. Phys*, 28(1):49, January 1957.

[12] Benedikt Johannes Scharfenberger. *Adiabatic Rapid Passage Sequences on Optically Pumped He-Atoms*. Master's thesis, State University of New York Stony Brook, August 2007.

[13] Robert Fisher, Haidong Yuan, Andreas Spoerl, and Steffen Glaser. Time-optimal generation of cluster states. *Phys. Rev. A*, 79(4, Part A), APR 2009. ISSN 1050-2947. doi: {10.1103/PhysRevA.79.042304}.

[14] Harold Metcalf and Peter van der Straten. *Laser Cooling and Trapping*. Springer-Verlag New York, 1999.

[15] M. Partlow. *Bichromatic Collimation to Make an Intense Helium Beam*. PhD thesis, Stony Brook University, 2004.

[16] V.S. Voitsekhovich, M.V. Danileiko, A.M. Negriiko, and V. Romanenko. Observation of a stimulated radiation pressure of amplitude-modulated light on atoms. *JETP Lett.*, 49:161–164, 1989.

[17] V.S. Voitsekhovich, M.V. Danileiko, A.M. Negriiko, V. Romanenko, and L. Yatsenko. Light pressure on atoms in counterpropagating amplitude-modulated waves. *Sov. Phys. Tech. Phys.*, 33:690–691, 1988.

[18] R. Grimm, J. Söding, and Yu. B. Ovchinnikov. Coherent beam splitter for atoms based on a bichromatic standing light-wave. *Opt. Lett.*, 19(9): 658–660, 1994.

[19] R. Grimm, G. Wasik, J. Söding, and Yu. B. Ovchinnikov. Laser cooling and trapping with rectified optical dipole forces. In A. Aspect, W. Barletta, and R. Bonifacio, editors, *Proceedings of the Fermi School CXXXI*, page 481. IOS Press, 1996.

[20] M. R. Williams, F. Chi, M. T. Cashen, and H. Metcalf. Bichromatic force measurements using atomic beam deflections. *Phys. Rev. A*, 61(2): 023408, Jan 2000. doi: 10.1103/PhysRevA.61.023408.

[21] J. Söding, R. Grimm, Yu. B. Ovchinnikov, P. Bouyer, and C. Salomon. Short-distance atomic-beam deceleration with a stimulated light force. *Phys. Rev. Lett.*, 78(8):1420–1423, 1997.

[22] M. Cashen and Harold Metcalf. Bichromatic force on helium. *Phys. Rev. A*, 63:025406, 2001.

[23] M. Cashen and Harold Metcalf. Optical forces on atoms in nonmonochromatic light. *J. Opt. Soc. Am. B*, 20:915, 2003.

[24] Claire Shean Allred. *Neutral Atom Lithography with Metastable Helium.* PhD thesis, Stony Brook University, 2009.

[25] S. S. Hodgman, R. G. Dall, L. J. Byron, K. G. H. Baldwin, S. J. Buckman, and A. G. Truscott. Metastable helium: A new determination of the longest atomic excited-state lifetime. *Phys. Rev. Lett.*, 103(5):053002, 2009.

[26] A. Abragam. *Principles of Nuclear Magnetism.* Oxford Universiy Press, Oxford, 2002.

[27] E. B. Treasy. Adiabatic inversion with light pulses. *Phys. Lett. A*, 27:421, 1968.

[28] M. M. T. Loy. Observation of population inversion by optical adiabatic rapid passage. *Phys. Rev. Lett.*, 32:814, 1974.

[29] L. Yatsenko, S. Guerin, and H. R. Jauslin. Topology of adiabatic passage. *Phys. Rev. A*, 65:043407, 2002.

[30] Tony Lu, Xiyue Miao, and Harold Metcalf. Bloch theorem on the bloch sphere. *Phys. Rev. A*, 2005.

[31] Tony Lu, Xiyue Miao, and Harold Metcalf. Nonadiabatic transitions in finite-time adiabatic rapid passage. *Phys. Rev. A*, 2007.

[32] D. Sawicki and Joseph H. Eberly. Perfect following in the adiabatic limit. *Optics Express*, 4(271), 1999.

[33] G. Demeter, G. P. Djotyan, Zs. Sörlei, and J. S. Bakos. Mechanical effect of retroreflected frequency-chirped laser pulses on two-level atoms. *Phys. Rev. A*, (74), 2006.

[34] J. Kawanaka, M. Hagiuda, K. Shimizu, and H. Takuma. Generation of an intense low-velocity metastable-neon atomic beam. *App. Phys. B*, (56(1)):21–24, 1993.

[35] M. Cashen. *Optical Forces on Atoms in Polychromatic Light Fields.* PhD thesis, Stony Brook University, 2002.

[36] W. Lu, M. D. Hoogerland, D. Milic, K. G. H. Baldwin, and S. J. Buckman. A bright metastable atom source at 80 k. *Rev. Sci. Instrum.*, 72:2558–61, 2001.

[37] W. Demtröder. *Laser Spectroscopy - Basic Concepts and Instrumentation.* Springer Verlag, Berlin, 3rd edition, 2003.

[38] C. Avila. *Spectral Control of a 1083 nm Diode Laser.* Master's thesis, Stony Brook University, 1998.

[39] A. Yariv. *Optical Electronics in Modern Communications.* Oxford Universiy Press, New York, 1997.

[40] G. B. Arfken and H. J. Weber. *Mathematical Methods for Physicists.* Academic Press, London, 1995.

Appendix A

Code

A.1 Definition of the Optical Bloch Equations

obeARP.h

```
/*
  author  benjamin glaessle
  email b_glaessle@gmx.net
  date  7/21/2009

  descr   definition of the optical bloch equations and
      their jacobians for the numeric integration by the GNU
      Scientific Library (GSL)

  features  spontaneous decay/emission on or off
        overlapping

*/

// definition of the system of differential equations (=the
    optical bloch equations themself)
int obe (double t, const double y[], double f[], void *
    params)
{
//  double gamma=((double *)params)[0]; // decay rate * 2 *
    pi
  double wM=((double *)params)[1];   // modulation-frequency
      = 2 * pulse frequency
  double w0=((double *)params)[2];   // Rabi-amplitude
```

```
//   double w1=((double *)params)[7];   // Rabi-amplitude
  double d0=((double *)params)[3];   // detuning-amplitude
  double kv=((double *)params)[4];   // doppler-detuning
  double T=((double *)params)[5];    // cycle time
  double tau=((double *)params)[6]; // delay time in units
      of T

  double t2=t-tau*T;

  double torque[3]={0.0,0.0,0.0};

  if(t/T - floor(t/T) <= .25) {
    torque[0]+=w0*sin(wM*t);
//      torque[1]+=w1*sin(wM*t);
    torque[2]+=-d0*cos(wM*t)+kv;
  }

  if(t2/T - floor(t2/T)<=.25) {
    torque[0]+=w0*sin(wM*t2);
//      torque[1]+=w1*sin(wM*t2);
    torque[2]+=ARP_UPDOWN*d0*cos(wM*t2)-kv;
  }

  f[0] = + torque[1]*y[2] - torque[2]*y[1];
  f[1] = - torque[0]*y[2] + torque[2]*y[0];
  f[2] = + torque[0]*y[1] - torque[1]*y[0];

  return GSL_SUCCESS;
}


// definition of the jacobian matrix of the system of diff.
    equations and the time derivatives
int jac (double t, const double y[], double *dfdy, double
    dfdt[], void *params)
{
//   double gamma=((double *)params)[0]; // decay rate * 2 *
    pi
  double wM=((double *)params)[1];   // modulation-frequency
  double w0=((double *)params)[2];   // Rabi-amplitude
//   double w1=((double *)params)[7];   // Rabi-amplitude
  double d0=((double *)params)[3];   // detuning-amplitude
  double kv=((double *)params)[4];   // doppler-detuning
```

```
  double T=((double *)params)[5];    // cycle time
  double tau=((double *)params)[6]; // delay time in units of T

  double t2=t-tau*T;

  double torque[3]={0.0,0.0,0.0};
  double dtorque[3]={0.0,0.0,0.0};

  if(t/T - floor(t/T) <= .25) {
    torque[0]+=w0*sin(wM*t);
//    torque[1]+=w1*sin(wM*t);
    torque[2]+=-d0*cos(wM*t)+kv;
    dtorque[0]+=w0*wM*cos(wM*t);
//    dtorque[1]+=w1*wM*cos(wM*t);
    dtorque[2]+=d0*wM*sin(wM*t);
  }

  if(t2/T - floor(t2/T)<=.25) {
    torque[0]+=w0*sin(wM*t2);
//    torque[1]+=w1*sin(wM*t2);
    torque[2]+=ARP_UPDOWN*d0*cos(wM*t2)-kv;
    dtorque[0]+=w0*wM*cos(wM*t2);
//    dtorque[1]+=w1*wM*cos(wM*t2);
    dtorque[2]+=-ARP_UPDOWN*d0*wM*sin(wM*t2);
  }

  gsl_matrix_view dfdy_mat = gsl_matrix_view_array (dfdy, 3, 3);
  gsl_matrix * m = &dfdy_mat.matrix;

  // jacobian matrix
  gsl_matrix_set (m, 0, 0, 0.0);
  gsl_matrix_set (m, 0, 1, -torque[2]);
  gsl_matrix_set (m, 0, 2, torque[1]);

  gsl_matrix_set (m, 1, 0, torque[2] );
  gsl_matrix_set (m, 1, 1, 0.0 );
  gsl_matrix_set (m, 1, 2, -torque[0] );

  gsl_matrix_set (m, 2, 0, -torque[1] );
  gsl_matrix_set (m, 2, 1, torque[0]);
  gsl_matrix_set (m, 2, 2, 0.0);
```

```
  // explicit time derivates
  dfdt[0] = dtorque[1]*y[2]-dtorque[2]*y[1];
  dfdt[1] = dtorque[2]*y[0]-dtorque[0]*y[2];
  dfdt[2] = dtorque[0]*y[1]-dtorque[1]*y[0];

  return GSL_SUCCESS;
}


int obeSD (double t, const double y[], double f[], void *
    params)
{
  double gamma=((double *)params)[0]; // decay rate * 2 * pi
  double wM=((double *)params)[1];  // modulation-frequency
      = 2 * pulse frequency
  double w0=((double *)params)[2];  // Rabi-amplitude
//  double w1=((double *)params)[7];  // Rabi-amplitude
  double d0=((double *)params)[3];  // detuning-amplitude
  double kv=((double *)params)[4];  // doppler-detuning
  double T=((double *)params)[5];   // cycle time
  double tau=((double *)params)[6]; // delay time in units
      of T

  double t2=t-tau*T;

  double torque[3]={0.0,0.0,0.0};

  if(t/T - floor(t/T) <= .25) {
    torque[0]+=w0*sin(wM*t);
//    torque[1]+=w1*sin(wM*t);
    torque[2]+=-d0*cos(wM*t)+kv;
  }

  if(t2/T - floor(t2/T)<=.25) {
    torque[0]+=w0*sin(wM*t2);
//    torque[1]+=w1*sin(wM*t2);
    torque[2]+=ARP_UPDOWN*d0*cos(wM*t2)-kv;
  }

  f[0] = -gamma/2*y[0] + torque[1]*y[2] - torque[2]*y[1];
  f[1] = -gamma/2*y[1] - torque[0]*y[2] + torque[2]*y[0];
  f[2] = -gamma*(1+y[2]) + torque[0]*y[1] - torque[1]*y[0];
```

```
  return GSL_SUCCESS;
}


// definition of the jacobian matrix of the system of diff. equations and the time derivatives
int jacSD (double t, const double y[], double *dfdy, double dfdt[], void *params)
{
  double gamma=((double *)params)[0]; // decay rate * 2 * pi
  double wM=((double *)params)[1];  // modulation-frequency
  double w0=((double *)params)[2];  // Rabi-amplitude
//  double w1=((double *)params)[7];  // Rabi-amplitude
  double d0=((double *)params)[3];  // detuning-amplitude
  double kv=((double *)params)[4];  // doppler-detuning
  double T=((double *)params)[5];   // cycle time
  double tau=((double *)params)[6]; // delay time in units of T

  double t2=t-tau*T;

  double torque[3]={0.0,0.0,0.0};
  double dtorque[3]={0.0,0.0,0.0};

  if(t/T - floor(t/T) <= .25) {
    torque[0]+=w0*sin(wM*t);
//    torque[1]+=w1*sin(wM*t);
    torque[2]+=-d0*cos(wM*t)+kv;
    dtorque[0]+=w0*wM*cos(wM*t);
//    dtorque[1]+=w1*wM*cos(wM*t);
    dtorque[2]+=d0*wM*sin(wM*t);
  }

  if(t2/T - floor(t2/T)<=.25) {
    torque[0]+=w0*sin(wM*t2);
//    torque[1]+=w1*sin(wM*t2);
    torque[2]+=ARP_UPDOWN*d0*cos(wM*t2)-kv;
    dtorque[0]+=w0*wM*cos(wM*t2);
//    dtorque[1]+=w1*wM*cos(wM*t2);
    dtorque[2]+=-ARP_UPDOWN*d0*wM*sin(wM*t2);
  }

```

```
  gsl_matrix_view dfdy_mat = gsl_matrix_view_array (dfdy, 3, 3);
  gsl_matrix * m = &dfdy_mat.matrix;

  // jacobian matrix
  gsl_matrix_set (m, 0, 0, -gamma/2);
  gsl_matrix_set (m, 0, 1, -torque[2]);
  gsl_matrix_set (m, 0, 2, torque[1]);

  gsl_matrix_set (m, 1, 0, torque[2] );
  gsl_matrix_set (m, 1, 1, -gamma/2 );
  gsl_matrix_set (m, 1, 2, -torque[0] );

  gsl_matrix_set (m, 2, 0, -torque[1]);
  gsl_matrix_set (m, 2, 1, torque[0]);
  gsl_matrix_set (m, 2, 2, -gamma);

  // explicit time derivates
  dfdt[0] = dtorque[1]*y[2]-dtorque[2]*y[1];
  dfdt[1] = dtorque[2]*y[0]-dtorque[0]*y[2];
  dfdt[2] = dtorque[0]*y[1]-dtorque[1]*y[0];

  return GSL_SUCCESS;
}
```

A.2 Numerical Integration

obe_arp_map_v0.5.cpp

```
/*
  author:    benjamin glaessle
  email:     b_glaessle@gmx.net
  altered:   12/10/08
  version:   0.5

  descr.:    Code used to map the force in ARP space (given by Omega0 & delta0),
             by straightforward evaluation of the optical bloch equations (obe).
```

```
        Uses correct parameters, not multiples of some other parameter.
        Sinussoidal pulses, Cosine chirping
        Ouput in files in subfolder

  uncomplete: commenting

  compiling:  g++ on Ubuntu using "cgsl" shell script
        basically universal code >> should work on other systems as well
*/

//
//    RUN PARAMETERS
//
#define ARP_OP     "kvScans/decayII/ud"  // "output folder/descr of the data"

#define ARP_N    500      // Number of pulses
#define ARP_INIT_N  0      // number of precalc. pulses which are done beforing calculating the force

#define ARP_STEPS 1000     // number of forced intermediate steps per cycle

#define ARP_UPDOWN  1      // chirp sequenz. 1 for up down/-1 for up up

// parameters in multiples of the modulation frequency ...
#define ARP_minRABI0  0.1
#define ARP_maxRABI0  5.0
#define ARP_dRABI0    0.1

#define ARP_minDET0   0.0
#define ARP_maxDET0   5.0
#define ARP_dDET0    0.1

#define ARP_maxKV    8.0
#define ARP_dKV      0.05

#define ARP_DELAY    0.25  // in units of one complete cycle, standard is .25
#define ARP_SD       true  // only symbolic
```

```
//
//      END: RUN PARAMETERS
//



#include "standard"          // consist of a collection of standard c++ libraries( like math, std, iostream, etc )
#include "cMeasurement.h"    // simply class to take data, and get the mean, variance, error, rms, etc

#include <gsl/gsl_errno.h>     // gsl = Gnu Scientfic Library
#include <gsl/gsl_matrix.h>
#include <gsl/gsl_odeiv.h>

#include "obeARP.h"          // definition of the optical bloch equations, with and without spontaneous decay (SD)

int main (void)
{
    // string and stringstream for variable file output by ofstream
  string sc;
  stringstream ds;
  ofstream os;

    // natural constants
//  const double hbar=1.05459E-34;
//  const double csol=299792458.0;

    // experimental constants
//  const double lambda=1083.0E-9;     // wavelength
  const double gamma=2.0*M_PI*1.6E6;  // decay rate * 2 * pi
//  const double kay=2.0*M_PI/lambda; // momentum
//  const double omegaA=csol/kay;    // circular frequency

    // experimental variables
  double OmegaM=100.*gamma;     // modulation-frequency
  double Omega0=ARP_minRABI0*OmegaM;   // Rabi-amplitude
  double delta0=ARP_minDET0*OmegaM;    // detuning-amplitude
  double kv=0.0;              // doppler-detuning
  double tau=ARP_DELAY;       // delay between the to counterpropagating pulses in units of TC
```

```
  double Tc=4.0*M_PI/OmegaM;      // cycle time = 2 modulation periods

    // array used for passing variables to the integrating routines
  double param[7]={gamma, OmegaM, Omega0, delta0, kv, Tc, ARP_DELAY};

    // definition of the integration method
  const gsl_odeiv_step_type * T = gsl_odeiv_step_rk8pd;
//  const gsl_odeiv_step_type * T = gsl_odeiv_step_gear1;
//  const gsl_odeiv_step_type * T = gsl_odeiv_step_gear2;
//  const gsl_odeiv_step_type * T = gsl_odeiv_step_bsimp;

  gsl_odeiv_step * s  = gsl_odeiv_step_alloc (T, 3);     // (method, dimension)
  gsl_odeiv_control * c  = gsl_odeiv_control_y_new (1e-8, 0.0); // (absolut accuracy, relative accuracy)
  gsl_odeiv_evolve * e = gsl_odeiv_evolve_alloc (3);     // (dimension)

//  gsl_odeiv_system sys= {obe, jac, 3, &param};
  gsl_odeiv_system sys= {obeSD, jacSD, 3, &param};

  int gslstatus;

  double t,ta,tb;         // running time variable
  double dt= Tc/ARP_STEPS;  // forced intermediate steps

//  double t1 = ARP_INIT_N*Tc;          // initialization time
  double t2 = (ARP_INIT_N + ARP_N)*Tc;  // simulation time

  double h = Tc*1e-6; // minimal stepsize.
  double y[3];
  double rr;

  double fcurr,fprev,ftemp; // variables for the forces
  Measurement f;

  double sw;     // switching parameter
  int mode=0;    // right(0)/left(1) propagating / deadtime (2)

```

```
  for( Omega0=ARP_minRABI0; Omega0<=ARP_maxRABI0; Omega0+= ARP_dRABI0 ) {
    param[2]=Omega0*OmegaM;

    for( delta0=ARP_minDET0; delta0 <=ARP_maxDET0; delta0 += ARP_dDET0 ) {
      param[3]=delta0*OmegaM;

      ds.str("");                                          // method
      ds << ARP_OP << "_N" << ARP_N << "wR" << Omega0 << "det" << delta0 << ".dat"; // to set variable
      sc = ds.str();                                       // filenames

      // open the file (don't know if it overwrites prevoiusly existing files with the same name)
      os.open(sc.data());
      if (not os)
      {
        cout << "file could not be opened. check if creation of the variable filename resulted in something not valid." << endl;
        return -1;
      }

      for( kv=-ARP_maxKV; kv <=ARP_maxKV; kv+= ARP_dKV) {
        param[4] = kv*OmegaM;

          // init
        t=0.0;
        y[0] = 0.0;
        y[1] = 0.0;
        y[2] = -1.0;  // problem -1 or -decay correct?

        f.Reset();
        fcurr=5.0;
        fprev=10.0;
        ftemp=0.0;

        mode=0;

        // data taking loop
```

```
        while (t < t2) {
          ta=t;
            // integration step!!!
          gslstatus = gsl_odeiv_evolve_apply (e, c, s,
                  &sys,
                  &t, t+dt,
                  &h, y);
          if (gslstatus != GSL_SUCCESS)
            break;

          // usefull
          rr = y[0]*y[0] + y[1]*y[1] + y[2]*y[2];
          sw=t/Tc - floor(t/Tc);
          tb=t-tau*Tc;

          // calculate and add the force from right
              propagating field
          if(sw <= .25)
            ftemp +=Omega0*OmegaM*sin(OmegaM*t)*y[1]*(t-ta);

          // calculate and add the force from left
              propagating field
          if(tb/Tc - floor(tb/Tc) <= .25)
            ftemp -=Omega0*OmegaM*sin(OmegaM*tb)*y[1]*(t-ta)
                ;

          // sort it out
          switch (mode) {
            case 0:
              if ( sw >=.50) {
               mode++;
              }
              break;
            case 1:
              if ( sw <.50) {
               mode=0;
               fprev=fcurr;
               fcurr=ftemp/2.0;
               f.Input(fcurr);
               ftemp=0.0;
              }
              break;
          }
```

```
        }
          // output the results into the defined files
        os << kv << " " << f.GetMean() << " " << f.
            GetVariance() << endl;
      }

      os.close(); // close the file
    }
  }

  gsl_odeiv_evolve_free (e);  // free memory
  gsl_odeiv_control_free (c);
  gsl_odeiv_step_free (s);

  return 0;
}


/*
//
//
//
*/
```